

Low Mach Number Modeling of Type Ia Supernovae. III. Reactions

A. S. Almgren¹, J. B. Bell¹, M. Zingale²

ABSTRACT

We complete the description of a low Mach number hydrodynamics algorithm suited to reacting, full star flows. Here we demonstrate how to accurately incorporate reactions using a second-order accurate Strang-splitting technique. We also discuss the modifications necessary to account for spherical self-gravitating stars. As with the previous implementation, we continue to allow for the expansion of the base state in response to heating, taking care to account for the compositional changes to the base state. The new algorithm is tested via comparisons with a fully compressible code and shown to be in good agreement. The resulting code, **MAESTRO**, will be used to study the convection and ignition phases of Type Ia supernovae.

Subject headings: supernovae: general — white dwarfs — hydrodynamics — nuclear reactions, nucleosynthesis, abundances — convection — methods: numerical

1. Introduction

In the generally accepted model of Type Ia supernovae (SNe Ia), a white dwarf accretes mass from a companion until it reaches the Chandrasehkar mass (see Hillebrandt & Niemeyer 2000 for a recent review). For centuries, subsonic convection (Mach number, M , ~ 0.01 to 0.1) transports heat generated at or near the center throughout the star (Baraffe et al. 2004; Woosley et al. 2004; Wunsch & Woosley 2004; Kuhlen et al. 2006). Only in the last second before the star unbinds does the Mach number approach, and possibly exceed, unity. It is the details of this convective phase that determine initial conditions for the subsequent explosion. Simulations have shown that different approximations for the initial conditions

¹Center for Computational Science and Engineering, Lawrence Berkeley National Laboratory, Berkeley, CA 94720

²Dept. of Physics & Astronomy, SUNY Stony Brook, Stony Brook, NY 11794-3800

lead to very different explosion behaviors (Niemeyer et al. 1996; Plewa et al. 2004; García-Senz & Bravo 2005; Livne et al. 2005; Röpke et al. 2006a,b). Efficient simulation of this convection requires modern numerical methods tuned to the conditions in the star. Other astrophysical environments, such as classical novae and X-ray bursts, are also characterized by low Mach number dynamics, and could benefit from the algorithm approach outlined below.

In this paper, we continue the development of a low Mach number hydrodynamics algorithm for astrophysical flows. As shown previously (see Almgren et al. 2006a—henceforth paper I, and Almgren et al. 2006b—henceforth paper II,), the low Mach number hydrodynamics system of equations accurately describes the typical flows in SNe Ia conditions for Mach numbers less than 0.2, providing a robust representation of finite-amplitude density and temperature perturbations and accurately capturing the expansion of the atmosphere due to heat release. Here, we add species advection with realistic burning networks to the previous framework. An underlying assumption in the low Mach number approximation is that the pressure remains close to the background pressure. In the presence of reactions, the heat release causes the background state to expand. As discussed in Almgren (2000) and demonstrated numerically in paper II for an externally specified heating profile, if the base state does not evolve in response to this heating, then the low Mach number method quickly becomes invalid. In this paper, we also discuss how to generalize the algorithm to spherical self-gravitating stars.

Recently, Lin et al. (2006) presented an alternate formulation of the low Mach number method for astrophysical flows with reactions, and demonstrated its utility in simulating Type I X-ray bursts. There are a number of differences between their algorithm and the one presented here. First, their method does not allow for base state expansion, and therefore is restricted to situations where the total energy release is not significant. In addition, the form in which the equations are solved numerically differs between the two algorithms. Low Mach number models, which include a constraint on the divergence of the velocity field, are typically integrated using a fractional step projection approach. In this approach, one first advances the system without satisfying the constraint. In the second step a discrete projection is then applied so that the low Mach number divergence constraint is satisfied. With this type of fractional step approach it is not possible to numerically conserve mass and energy (or enthalpy) while simultaneously satisfying the equation of state. In Lin et al. (2006) the temperature is evolved and the equation of state is used to find the new density. Instead, we solve conservative equations for both density and enthalpy, and relax the equation of state. The second major difference between our approach and that of Lin et al. relates to the projection step of the algorithm. Lin et al. formulate a projection algorithm in terms of a constant-coefficient pressure-Poisson equation, derived from the mass conservation equation,

to be solved at each time step. In contrast, we define the projection as an orthogonal decomposition of velocity in a weighted inner-product space. While our approach leads to a somewhat more expensive variable-coefficient elliptic solve, it has the advantage that it can handle larger density contrasts without encountering stability issues (see Bell & Marcus (1992), Almgren et al. (1998) and Sussman et al. (1999)) and has been shown to have better convergence properties (see Nicoud (2000)). Finally, our method is based on a second-order accurate discretization in space and time.

With the algorithm presented in this paper we plan to simulate the convection that precedes the explosion of the white dwarf, in order to understand how ignition occurs. Other algorithms have been used in the literature to study this problem, including an implicit method (Höflich & Stein 2002) and the anelastic approximation (Kuhlen et al. 2006). Few details are provided about the implicit algorithm used by Höflich & Stein (2002), so it is difficult to compare to our new algorithm. Direct comparisons with the anelastic method, presented in paper I, showed that at low Mach numbers and small deviations of temperature and density from the background state, the low Mach number method and the anelastic method agree well. The low Mach number method continues to be valid for large density and temperature perturbations where the anelastic formulation breaks down. We plan to follow the evolution of the convection through the development of finite-amplitude hot spots, as well as capture the expansion of the white dwarf as it is heated by the reactions at the center.

In § 2 we discuss the low Mach number equation set with a reaction network. In § 3 the numerical methodology is explained in detail. Results are in § 4, including comparisons to a fully compressible code and convergence tests. We conclude in § 5.

2. Low Mach Number Hydrodynamics

In paper II, we derived a system of low Mach number equations for stellar atmospheres with a time-dependent background state that depended on externally prescribed heat sources. In this paper we generalize the low Mach number equation set from paper II to include reaction networks. The necessary assumption for validity of the generalized system is, as before, that the Mach number (M) of the flow be small. Then we can decompose the pressure, $p(\mathbf{x}, t)$, into a base state pressure, $p_0(r, t)$, and a perturbational, or dynamic, pressure, $\pi(\mathbf{x}, t)$, such that $|\pi|/p_0 = O(M^2)$. The perturbations of density and temperature need not be small. The base state is assumed to be in hydrostatic equilibrium, i.e., $\nabla p_0 = -\rho_0 g \mathbf{e}_r$, where ρ_0 is the base state density, and \mathbf{e}_r is the unit vector in the radial direction.

We recall from paper I the fully compressible equations of motion in a stellar environment with species evolution equations and reaction terms.

$$\frac{\partial \rho}{\partial t} + \nabla \cdot (\rho \mathbf{U}) = 0 , \quad (1)$$

$$\frac{\partial(\rho \mathbf{U})}{\partial t} + \nabla \cdot (\rho \mathbf{U} \mathbf{U}) + \nabla p = -\rho g \mathbf{e}_r , \quad (2)$$

$$\frac{\partial(\rho h)}{\partial t} + \nabla \cdot (\mathbf{U} \rho h) = \frac{Dp}{Dt} - \sum_k \rho q_k \dot{\omega}_k + \rho H_{\text{ext}} , \quad (3)$$

$$\frac{\partial(\rho X_k)}{\partial t} + \nabla \cdot (\mathbf{U} \rho X_k) = \rho \dot{\omega}_k \quad (4)$$

where ρ , \mathbf{U} , h , and p are the density, velocity, enthalpy, and pressure, respectively. Here we have written the energy equation in terms of enthalpy rather than total energy, as in paper I. The species are represented by their mass fractions, X_k along with their associated production rates, $\dot{\omega}_k$, and binding energies, q_k . Equation (1), the mass equation, and equation (4), the species equations, are degenerate, since

$$\sum_k X_k = 1 ,$$

and therefore by definition

$$\sum_k \dot{\omega}_k = \frac{D}{Dt} \sum_k X_k = 0 .$$

For generality we retain the external heat source, H_{ext} , from paper II. Formally, the gravitational acceleration, $g(r)$, is found from the gravitational potential, Φ , via $\mathbf{g} = -\nabla \Phi$, where Φ satisfies Poisson's equation,

$$\nabla^2 \Phi = 4\pi G \rho .$$

Finally, the system is closed with the equation of state

$$p = p(\rho, h, X_k) .$$

As in our previous work, we use a general stellar equation of state with contributions from ions, radiation, and electron degeneracy (Timmes & Swesty 2000).

We now derive the low Mach number equation set in a manner analogous to the derivation in paper II, but with species and reaction terms added. We rewrite conservation of mass as an expression for the divergence of velocity:

$$\nabla \cdot \mathbf{U} = -\frac{1}{\rho} \frac{D\rho}{Dt} . \quad (5)$$

Differentiating the equation of state, written in the form, $p = p(\rho, T, X_k)$, along particle paths, we can write

$$\frac{D\rho}{Dt} = \frac{1}{p_\rho} \left(\frac{Dp}{Dt} - p_T \frac{DT}{Dt} - \sum_k p_{X_k} \dot{\omega}_k \right) , \quad (6)$$

with $p_\rho = \partial p / \partial \rho|_{X_k, T}$, $p_{X_k} = \partial p / \partial X_k|_{T, \rho, (X_j, j \neq k)}$, and $p_T = \partial p / \partial T|_{\rho, X_k}$.

An expression for DT/Dt can be found by applying the chain rule for $h = h(p, T, X_k)$ to the enthalpy equation (Eq. [3]):

$$\frac{DT}{Dt} = \frac{1}{\rho c_p} \left[(1 - \rho h_p) \frac{Dp}{Dt} - \sum_k \rho \xi_k \dot{\omega}_k - \sum_k \rho q_k \dot{\omega}_k + \rho H_{\text{ext}} \right] , \quad (7)$$

where $c_p = \partial h / \partial T|_{p, X_k}$ is the specific heat at constant pressure, $h_p \equiv \partial h / \partial p|_{T, X_k}$, and $\xi_k \equiv \partial h / \partial X_k|_{T, p, (X_j, j \neq k)}$ for convenience. Combining equations (5), (6), and (7), and replacing p by $p_0(r, t)$, we arrive at the divergence constraint on the velocity field

$$\nabla \cdot \mathbf{U} + \alpha \left(\frac{\partial p_0}{\partial t} + \mathbf{U} \cdot \nabla p_0 \right) = -\sigma \sum_k (\xi_k + q_k) \dot{\omega}_k + \frac{1}{\rho p_\rho} \sum_k p_{X_k} \dot{\omega}_k + \sigma H_{\text{ext}} \equiv S , \quad (8)$$

where

$$\alpha(\rho, T) \equiv - \left[\frac{(1 - \rho h_p) p_T - \rho c_p}{\rho^2 c_p p_\rho} \right] = \frac{1}{\Gamma_1 p_0} , \quad (9)$$

$\Gamma_1 \equiv d(\log p)/d(\log \rho)$ at constant entropy, and $\sigma \equiv p_T/(\rho c_p p_\rho)$. As in papers I and II, we evaluate Γ_1 at the base state, i.e., we set $\Gamma_1 = \Gamma_{10}$. The variation of Γ_1 is explored in the numerical tests presented in § 4.2 to ensure that the assumption continues to be reasonable. We note that the source term, S , is the same as that in our small-scale low Mach number astrophysical combustion algorithm (Bell et al. 2004), with the absence of thermal conduction and the addition of an explicit heating term. (We also note that we have changed our notation from paper I and II, from \tilde{S} to S . This is consistent with Bell et al. (2004).) We recall from papers I and II that this constraint can be written as

$$\nabla \cdot (\beta_0 \mathbf{U}) = \beta_0 \left(S - \alpha \frac{\partial p_0}{\partial t} \right) , \quad (10)$$

where

$$\beta_0(r, t) = \beta(0, t) \exp \left(\int_0^r \frac{1}{(\Gamma_1 p)_0} \frac{\partial p_0}{\partial r'} dr' \right) . \quad (11)$$

Summarizing the reacting low Mach number equation set, we have

$$\frac{\partial(\rho X_k)}{\partial t} = -\nabla \cdot (\mathbf{U} \rho X_k) + \rho \dot{\omega}_k ,$$

$$\frac{\partial(\rho h)}{\partial t} = -\nabla \cdot (\mathbf{U}\rho h) + \frac{Dp_0}{Dt} - \sum_k \rho q_k \dot{\omega}_k + \rho H_{\text{ext}} , \quad (12)$$

$$\begin{aligned} \frac{\partial \mathbf{U}}{\partial t} &= -\mathbf{U} \cdot \nabla \mathbf{U} - \frac{1}{\rho} \nabla \pi - \frac{(\rho - \rho_0)}{\rho} g \mathbf{e}_r , \\ \nabla \cdot (\beta_0 \mathbf{U}) &= \beta_0 \left(S - \frac{1}{\Gamma_{10} p_0} \frac{\partial p_0}{\partial t} \right) , \end{aligned} \quad (13)$$

where the total mass density is defined as

$$\rho = \sum_k \rho X_k , \quad (14)$$

and

$$S = -\sigma \sum_k (\xi_k + q_k) \dot{\omega}_k + \frac{1}{\rho p_\rho} \sum_k p_{X_k} \dot{\omega}_k + \sigma H_{\text{ext}} . \quad (15)$$

The major difference in the constraint considered in this paper relative to paper II is the form of S . Now, in addition to the external heat source, there is a reaction heat source (the term proportional to q_k), and compressibility terms due solely to compositional changes (the terms proportional to ξ_k and p_{X_k}). Here, $\dot{\omega}_k$ is evaluated by integrating the reaction network. The thermodynamic derivatives with respect to X_k are discussed in Appendix A.

We recall from paper II that we can decompose the full velocity field, \mathbf{U} , into a base state velocity, $w_0 \mathbf{e}_r$, and the remaining velocity field, $\tilde{\mathbf{U}}$, that governs the more local dynamics, i.e.,

$$\mathbf{U}(\mathbf{x}, r, t) = w_0(r, t) \mathbf{e}_r + \tilde{\mathbf{U}}(\mathbf{x}, r, t) , \quad (16)$$

where $\tilde{\mathbf{U}}$ satisfies

$$\int_{\Omega_H} \tilde{\mathbf{U}} \cdot \mathbf{e}_r dA = 0 ,$$

where Ω_H is a region at constant height for the plane-parallel atmosphere and at constant radius for the spherical geometry. Following this decomposition through in the manner of paper II, our equations for the species and enthalpy become

$$\frac{\partial(\rho X_k)}{\partial t} = -\nabla \cdot (\rho X_k \tilde{\mathbf{U}}) - \nabla \cdot (\rho X_k w_0 \mathbf{e}_r) + \rho \dot{\omega}_k , \quad (17)$$

$$\begin{aligned} \frac{\partial(\rho h)}{\partial t} &= -\nabla \cdot (\rho h \tilde{\mathbf{U}}) - \nabla \cdot (\rho h w_0 \mathbf{e}_r) + \left(\frac{\partial p_0}{\partial t} + w_0 \frac{\partial p_0}{\partial r} \right) \\ &\quad + (\tilde{\mathbf{U}} \cdot \mathbf{e}_r) \frac{\partial p_0}{\partial r} - \sum_k \rho q_k \dot{\omega}_k + \rho H_{\text{ext}} . \end{aligned} \quad (18)$$

As in paper II, we can separate the divergence constraint into that governing $\tilde{\mathbf{U}}$ and that governing w_0 , resulting in the expression

$$\nabla \cdot (\beta_0 w_0 \mathbf{e}_r) = \beta_0 \left(\bar{S} - \frac{1}{\Gamma_1 p_0} \frac{\partial p_0}{\partial t} \right) , \quad (19)$$

with

$$\bar{S}(r) = \frac{1}{A(\Omega_H)} \int_{\Omega_H} S \, d\mathbf{A} \, , \quad (20)$$

where $A(\Omega_H) \equiv \int_{\Omega_H} d\mathbf{A}$ and $d\mathbf{A}$ represents an area measure. In paper II, we showed that for the case of a plane-parallel subregion of the stellar atmosphere with constant gravity this reduced to

$$\frac{\partial w_0}{\partial r} = \bar{S} \, . \quad (21)$$

For the case of a spherical self-gravitating star, w_0 is determined by integrating

$$\frac{\partial}{\partial r} \left[\frac{\Gamma_{10} p_0}{r^2} \frac{\partial}{\partial r} (r^2 w_0) \right] = \frac{\partial(\Gamma_{10} p_0 \bar{S})}{\partial r} - \frac{4w_0 \rho_0 g(r)}{r} \, , \quad (22)$$

as derived in Appendix B.

Given w_0 we can update the base-state species,

$$\frac{\partial(\rho X_k)_0}{\partial t} = -\nabla \cdot [(\rho X_k)_0 w_0 \mathbf{e}_r] + \overline{\rho \dot{w}_k} \, , \quad (23)$$

where we define the average species mass creation rate, $\overline{\rho \dot{w}_k}$,

$$\overline{\rho \dot{w}_k} = \frac{1}{A(\Omega_H)} \int_{\Omega_H} (\rho \dot{w}_k) \, d\mathbf{A} \, . \quad (24)$$

We note that

$$\sum_k \overline{\rho \dot{w}_k} = \frac{1}{A(\Omega_H)} \sum_k \int_{\Omega_H} (\rho \dot{w}_k) \, d\mathbf{A} = 0 \, . \quad (25)$$

The base-state total mass density is simply

$$\rho_0 = \sum_k (\rho X_k)_0 \quad (26)$$

which we can show, by summation over equation (23) and the use of equation (25), satisfies

$$\frac{\partial \rho_0}{\partial t} = -\nabla \cdot (\rho_0 w_0 \mathbf{e}_r) \, , \quad (27)$$

as in paper II. Finally the pressure is updated by rearranging equation (19) once w_0 is known,

$$\frac{1}{\Gamma_{10} p_0} \frac{\partial p_0}{\partial t} = \bar{S} - \frac{1}{\beta_0} \nabla \cdot (\beta_0 w_0 \mathbf{e}_r) \, . \quad (28)$$

We define the Lagrangian derivative, D_0/Dt , which represents the change due only to evolution of the base state, i.e.,

$$\frac{D_0}{Dt} \equiv \frac{\partial}{\partial t} + w_0 \frac{\partial}{\partial r} \, .$$

We then define η as the Lagrangian change in the base-state pressure due to the base state expansion,

$$\begin{aligned}\eta \equiv \frac{D_0 p_0}{Dt} &= \frac{\partial p_0}{\partial t} + w_0 \frac{\partial p_0}{\partial r} \\ &= \Gamma_{10} p_0 (\bar{S} - \nabla \cdot (w_0 \mathbf{e}_r)) \quad .\end{aligned}\tag{29}$$

As discussed in paper II, $\eta = 0$ for a plane-parallel atmosphere with constant gravity. For a spherical self-gravitating star, $\eta \neq 0$ (see Appendix B), so we retain it for completeness.

We also need a base state enthalpy equation. One approach is to follow the ideas presented in paper II, and derive an evolution equation for the base state enthalpy by considering the full Lagrangian derivative of $h_0 = h(\rho_0, p_0, X_{k0})$. This results in a base state enthalpy equation that is thermodynamically consistent with the other base state quantities. We note, however, that unlike the base state pressure, p_0 , and density, ρ_0 , the base state enthalpy plays no role in the underlying formulation of the low Mach number approximation. The need for a base state enthalpy equation stems from the desire to write the state equations in perturbational form to reduce discretization errors. This means that we can use any reasonable choice of the base state enthalpy to define the perturbational enthalpy. Here we consider an alternative approach based on simply laterally averaging the full enthalpy equation:

$$\frac{\partial(\rho h)_0}{\partial t} = -\nabla \cdot [(\rho h)_0 w_0] + \eta - \sum_k q_k \overline{\rho \dot{\omega}_k} + \overline{\rho H_{\text{ext}}}\tag{30}$$

This more naturally parallels the base state species equations. In the algorithm presented here, we use this state to define the perturbational enthalpy but emphasize that h_0 is not thermodynamically consistent with the other base state quantities.

With the base state evolution equations defined, we can now write the perturbational form of equations (17) and equation (18) by subtracting off the appropriate base state equation:

$$\frac{\partial(\rho X_k)'}{\partial t} = -\nabla \cdot [(\rho X_k)'(\tilde{\mathbf{U}} + w_0 \mathbf{e}_r)] - \nabla \cdot [(\rho X_k)_0 \tilde{\mathbf{U}}] + (\rho \dot{\omega}_k - \overline{\rho \dot{\omega}_k})\tag{31}$$

$$\begin{aligned}\frac{\partial(\rho h)'}{\partial t} &= -\nabla \cdot [(\rho h)'(\tilde{\mathbf{U}} + w_0 \mathbf{e}_r)] - \nabla \cdot [(\rho h)_0 \tilde{\mathbf{U}}] + (\tilde{\mathbf{U}} \cdot \mathbf{e}_r) \frac{\partial p_0}{\partial r} \\ &\quad - \sum_k q_k (\rho \dot{\omega}_k - \overline{\rho \dot{\omega}_k}) + (\rho H_{\text{ext}} - \overline{\rho H_{\text{ext}}}) \quad ,\end{aligned}\tag{32}$$

where $(\rho X_k)' \equiv (\rho X_k) - (\rho X_k)_0$ and $(\rho h)' \equiv (\rho h) - (\rho h)_0$. Again, we define the perturbational mass density as

$$\rho' = \sum_k (\rho X_k)' \quad ,\tag{33}$$

which is equivalently,

$$\rho' = \rho - \rho_0 \ .$$

In writing the evolution of the velocity field, we make a slight correction to the equation given in paper II. In equation (23) of paper II we incorrectly split the dynamics between $\tilde{\mathbf{U}}$ and w_0 ; in effect we neglected the perturbational pressure term that appears in the evolution of w_0 , resulting in

$$\frac{\partial \tilde{\mathbf{U}}}{\partial t} = -\tilde{\mathbf{U}} \cdot \nabla \tilde{\mathbf{U}} - w_0 \frac{\partial \tilde{\mathbf{U}}}{\partial r} - \tilde{\mathbf{U}} \cdot \mathbf{e}_r \frac{\partial w_0}{\partial r} - \frac{1}{\rho} \nabla \pi - \frac{(\rho - \rho_0)}{\rho} g \mathbf{e}_r \ . \quad (34)$$

Here, after correctly splitting the dynamics, we have instead

$$\frac{\partial w_0}{\partial t} = -w_0 \frac{\partial w_0}{\partial r} - \frac{1}{\rho_0} \frac{\partial \pi_0}{\partial r} \ , \quad (35)$$

$$\frac{\partial \tilde{\mathbf{U}}}{\partial t} = -\tilde{\mathbf{U}} \cdot \nabla \tilde{\mathbf{U}} - w_0 \frac{\partial \tilde{\mathbf{U}}}{\partial r} - \tilde{\mathbf{U}} \cdot \mathbf{e}_r \frac{\partial w_0}{\partial r} - \frac{1}{\rho} \nabla \pi + \frac{1}{\rho_0} \frac{\partial \pi_0}{\partial r} - \frac{(\rho - \rho_0)}{\rho} g \mathbf{e}_r \ , \quad (36)$$

where we have introduced a new pressure term, π_0 . This term represents the dynamic pressure that shifts the base state. Similarly to π , the magnitude of π_0 is such that $|\pi_0|/|p_0| = O(M_0^2)$, where $M_0 = |w_0|/c$, so we can neglect its effect on thermodynamic relations.

We note that we actually calculate w_0 exactly as in paper II, since we use the one-dimensional divergence constraint (equation (19) or (20), as appropriate) to integrate w_0 , and this is unchanged. Then π_0 follows easily by integrating

$$-\frac{1}{\rho_0} \frac{\partial \pi_0}{\partial r} = \frac{\partial w_0}{\partial t} + w_0 \frac{\partial w_0}{\partial r} \ , \quad (37)$$

once w_0 at the old and new times is known, and the advective term is computed explicitly.

The constraint equation for $\tilde{\mathbf{U}}$ remains as in paper II:

$$\nabla \cdot (\beta_0 \tilde{\mathbf{U}}) = \beta_0 (S - \bar{S}) \ . \quad (38)$$

3. Numerical Methodology

The numerical methodology in this paper is more complicated than that outlined in paper II because of the need to integrate the reaction network. Again, we use a predictor-corrector formalism. In the predictor step we compute an estimate of the expansion of the base state, then compute an estimate of the state at the new time level. In the corrector step we use the results of the previous state update to compute a new base state update as well as full state update. For the base state and full state updates, we adopt a fractional-step method, using Strang-splitting of the reactions to achieve second-order accuracy in time.

3.1. Notation

We will make use of the following shorthand notations in outlining the algorithm:

- For any quantity, ϕ , we define $\bar{\phi} = \mathbf{Avg}(\phi)$, the average over Ω_H , as

$$\bar{\phi}(r) = \frac{1}{A(\Omega_H)} \int_{\Omega_H} \phi(r, \mathbf{x}) d\mathbf{A} . \quad (39)$$

- We define **React State** $(X_k^{\text{in}}, \rho^{\text{in}}, (\rho h)^{\text{in}}) \rightarrow (X_k^{\text{out}}, \rho^{\text{out}}, (\rho h)^{\text{out}}, (\rho \dot{\omega}_k)^{\text{out}})$ as the process by which we evolve the reactions from $X_k^{\text{in}} \rightarrow X_k^{\text{out}}$ by solving the following system of equations over a time interval of $\Delta t/2$:

$$\frac{dX_k}{dt} = \dot{\omega}_k(X_k, T) \quad (40)$$

$$\frac{dT}{dt} = -\frac{1}{c_p} \left[\sum_k (\xi_k + q_k) \dot{\omega}_k \right] \quad (41)$$

using the stiff ODE integration methods provided by the **VODE** package (Brown et al. 1989). The absolute error tolerances are set to 10^{-12} for the species and a relative tolerance of 10^{-5} is used for the temperature. The integration yields the new values of the mass fractions, X_k^{out} . Equation (41) is derived from equation (7) by assuming that the pressure is constant during the burn state. The initial temperature for integrating equation (41) is determined from $\rho^{\text{in}}, h^{\text{in}} = (\rho h)^{\text{in}}/\rho^{\text{in}}$ and X_k^{in} . We note that this temperature is used only to compute the reaction rates in equation (40), not to compute the final change in enthalpy. In evolving this equation, we need to evaluate c_p and ξ_k . In theory, this means evaluating the equation of state for each right-hand-side evaluation that **VODE** requires. In practice, we freeze these values at the start of the integration time step.

This step also incorporates the external heating, H_{ext} , treated here as a specified source term in the enthalpy equation. The enthalpy is updated by

$$(\rho h)^{\text{out}} = (\rho h)^{\text{in}} - \sum_k \rho^{\text{in}} (X_k^{\text{out}} - X_k^{\text{in}}) q_k + \frac{\Delta t}{2} (\rho^{\text{in}} H_{\text{ext}}) , \quad (42)$$

and we define

$$(\rho \dot{\omega}_k)^{\text{out}} = \frac{\rho^{\text{in}} (X_k^{\text{out}} - X_k^{\text{in}})}{\Delta t/2} . \quad (43)$$

The pressure and density remain unchanged during the **React State** step. Overall, this step performs an update of

$$\frac{\partial X_k}{\partial t} = \dot{\omega}_k$$

$$\frac{\partial(\rho h)}{\partial t} = - \sum_k q_k \rho \dot{\omega}_k + \rho H_{\text{ext}}$$

- **React Base** $((\rho X_k)_0^{\text{in}}, \rho_0^{\text{in}}, p_0^{\text{in}}, (\overline{\rho \dot{\omega}_k})^{\text{in}}, (\overline{\rho H_{\text{ext}}})^{\text{in}}) \rightarrow ((\rho X_k)_0^{\text{out}}, \rho_0^{\text{out}}, (\rho h)_0^{\text{out}}, p_0^{\text{out}}, \Gamma_{10}^{\text{out}}, \beta_0^{\text{out}})$.

This differs from the above reaction step in that we do not actually compute reactions in this step. Rather, we use the averaged reaction rate as input to update the species and enthalpy through $\Delta t/2$.

$$\begin{aligned} (p_0)^{\text{out}} &= (p_0)^{\text{in}} , \\ (\rho X_k)_0^{\text{out}} &= (\rho X_k)_0^{\text{in}} + \frac{\Delta t}{2} (\overline{\rho \dot{\omega}_k})^{\text{in}} , \end{aligned} \tag{44}$$

$$(\rho h)_0^{\text{out}} = (\rho h)_0^{\text{in}} - \frac{\Delta t}{2} \sum_k q_k (\overline{\rho \dot{\omega}_k})^{\text{in}} + \frac{\Delta t}{2} (\overline{\rho H_{\text{ext}}})^{\text{in}} , \tag{45}$$

$$\begin{aligned} \Gamma_{10}^{\text{out}} &= \Gamma_1(\rho_0^{\text{out}}, p_0^{\text{out}}, X_k^{\text{out}}) , \\ \beta_0^{\text{out}} &= \beta(\rho_0^{\text{out}}, p_0^{\text{out}}, \Gamma_{10}^{\text{out}}) , \end{aligned}$$

where $\rho_0^{\text{out}} = \rho_0^{\text{in}}$ since ρ does not change during the chemistry step, and $X_k^{\text{out}} = (\rho X_k)_0^{\text{out}} / \rho_0^{\text{out}}$.

We note that this is an explicit discretization of

$$\begin{aligned} \frac{\partial(\rho X_k)_0}{\partial t} &= \overline{\rho \dot{\omega}_k} \\ \frac{\partial(\rho h)_0}{\partial t} &= - \sum_k q_k (\overline{\rho \dot{\omega}_k}) + (\overline{\rho H_{\text{ext}}}) \end{aligned}$$

over an interval of $\Delta t/2$.

- **Advect Base** $(\rho_0^{\text{in}}, p_0^{\text{in}}, (\rho X_k)_0^{\text{in}}, (\rho h)_0^{\text{in}}, \beta_0^{\text{in}}, w_0^{\text{in}}) \rightarrow (\rho_0^{\text{out}}, p_0^{\text{out}}, (\rho X_k)_0^{\text{out}}, (\rho h)_0^{\text{out}}, \beta_0^{\text{out}})$ is the process by which we update the base state through Δt in time given the radial velocity w_0^{in} . Here we discuss the algorithm for plane-parallel geometries. The modifications necessary to treat spherical self-gravitating stars are presented in Appendix B. Regardless of the geometry, the base state pressure, density, species, enthalpy, and source term are defined at the cell centers, and the base state velocity, w_0 , and β_0 are defined at the interfaces.

1. Species and Density Update:

The first step is to update the base state species, using

$$(\rho X_k)_{0,j}^{\text{out}} = (\rho X_k)_{0,j}^{\text{in}} - \frac{\Delta t}{\Delta r} \left\{ [(\rho X_k)_0^{\text{in}, n+1/2} w_0^{\text{in}}]_{j+1/2} - [(\rho X_k)_0^{\text{in}, n+1/2} w_0^{\text{in}}]_{j-1/2} \right\}$$

where j refers to the one-dimensional index in the radial direction. The interface states are found via the procedure described in paper II, Appendix A. We then update the base state density,

$$\rho_0^{\text{out}} = \sum_k (\rho X_k)_0^{\text{out}} .$$

2. Pressure Update:

The pressure update proceeds as in paper II:

$$p_{0,j}^{\text{out}} = p_{0,j}^{\text{in}} - \frac{\Delta t}{2\Delta r} \left(w_{0,j+1/2}^{\text{in}} + w_{0,j-1/2}^{\text{in}} \right) \left(p_{0,j+1/2}^{\text{in},n+1/2} - p_{0,j-1/2}^{\text{in},n+1/2} \right) \quad (46)$$

where the interface states are again found via the procedure described in paper II, Appendix A. We note this is a discretization of $\partial p_0 / \partial t = -w_0 \partial p_0 / \partial r$, which follows from equation (29) with $\eta = 0$ for the plane-parallel case.

3. Enthalpy Update:

After the base state species and pressure are updated, we compute the updated base state enthalpy,

$$(\rho h)_{0,j}^{\text{out}} = (\rho h)_{0,j}^{\text{in}} - \frac{\Delta t}{\Delta r} \left\{ [(\rho h)_0^{\text{in},n+1/2} w_0^{\text{in}}]_{j+1/2} - [(\rho h)_0^{\text{in},n+1/2} w_0^{\text{in}}]_{j-1/2} \right\} \quad (47)$$

The update to $(\rho h)_0$ is a discretization over an interval of Δt of

$$\frac{\partial (\rho h)_0}{\partial t} = -\nabla \cdot [(\rho h)_0 w_0] ,$$

i.e., equation (30) without the terms due to heating or reactions, and $\eta = 0$. Finally, using the equation of state, we now compute

$$\Gamma_{10}^{\text{out}} = \Gamma_1(\rho_0^{\text{out}}, p_0^{\text{out}}, X_{k0}^{\text{out}}) ,$$

and use this to construct

$$\beta_0^{\text{out}} = \beta_0(g^{\text{out}}, \Gamma_{10}^{\text{out}}, p_0^{\text{out}}) .$$

The computation of β_0 is detailed in Appendix C.

3.2. Time-Advancement Algorithm

We now describe the full time advancement algorithm, making frequent use of the shorthand developed above. Here, we assume that the problem is already properly initialized. We describe the details of the initialization in the next subsection.

Step 1 Define the average expansion at time $t^{n+1/2}$ and the new w_0 .

- a. At the beginning of each time step, we need an estimate for the time-centered source term in our constraint equation, equation (8). If this is the first step of the calculation ($n = 0$), we set

$$S^{1/2,\star} = \frac{1}{2}(S^0 + S^1) ,$$

where S^1 is found through the iterative process that initializes the calculation. Otherwise, following the method used in our small-scale low Mach number algorithm (Bell et al. 2004), we extrapolate to the half-time using the source terms at the previous and current time levels:

$$S^{n+1/2,\star} = S^n + \frac{\Delta t^n}{2} \frac{S^n - S^{n-1}}{\Delta t^{n-1}} . \quad (48)$$

- b. Define

$$\overline{S}^{n+1/2,\star} = \mathbf{Avg}(S^{n+1/2,\star}) .$$

- c. Define $w_0^{n+1/2,\star}$ using $\overline{S}^{n+1/2,\star}$ by solving equation (22) as described in Appendix B for spherical configurations, or by solving equation (21) for plane-parallel geometries. In the case of spherical geometries use the current p_0^n , $\Gamma_{10}^n = \Gamma_1(p_0^n, \rho_0^n, X_k^n)$, and g as computed from ρ_0^n .

- d. Using equation (37), define

$$-\left(\frac{1}{\rho_0} \frac{\partial \pi_0}{\partial r}\right) = \frac{w_0^{n+1/2,\star} - w_0^{n-1/2}}{\Delta t} + \left(w_0 \frac{\partial w_0}{\partial r}\right)^{n+1/2,\star} \quad (49)$$

Step 2 *Construct the advective velocity, \mathbf{U}^{ADV} :*

As in paper II, predict a time-centered, second-order accurate, staggered-grid approximation to \mathbf{U} , $\mathbf{U}^{\text{ADV},\star}$, using an unsplit Godunov method (Colella 1990) to approximate $\tilde{\mathbf{U}}$ at time $t^{n+1/2}$:

$$\begin{aligned} \mathbf{U}^{\text{ADV},\star} = \tilde{\mathbf{U}}^n &+ \frac{\Delta t}{2} \left\{ - \left[(\tilde{\mathbf{U}} + w_0^{n+1/2,\star} \mathbf{e}_r) \cdot \nabla \tilde{\mathbf{U}} \right]^{n+1/2} - (\tilde{\mathbf{U}} \cdot \mathbf{e}_r) \frac{\partial}{\partial r} w_0^{n+1/2,\star} \mathbf{e}_r \right\} \\ &+ \frac{\Delta t}{2} \left[-\frac{1}{\rho^n} \nabla \pi^{n-1/2} + \left(\frac{1}{\rho_0} \frac{\partial \pi_0}{\partial r} \right) - \frac{(\rho^n - \rho_0^n)}{\rho^n} g \mathbf{e}_r \right] \end{aligned}$$

The details for construction of $[(\tilde{\mathbf{U}} + w_0^{n+1/2,\star} \mathbf{e}_r) \cdot \nabla \tilde{\mathbf{U}}]^{n+1/2}$ are given in Appendix B of paper II, with $\mathbf{V} = \tilde{\mathbf{U}} + w_0^{n+1/2,\star} \mathbf{e}_r$. The construction of $(\tilde{\mathbf{U}} \cdot \mathbf{e}_r) \partial w_0^{n+1/2,\star} / \partial r$ is done analogously. We enforce the divergence constraint by solving

$$D^{\text{MAC}} \left(\frac{\beta_0^n}{\rho^n} G^{\text{MAC}} \phi^{\text{MAC}} \right) = D^{\text{MAC}} (\beta_0^n \mathbf{U}^{\text{ADV},\star}) - \beta_0^n (S^{n+1/2,\star} - \overline{S}^{n+1/2,\star}) . \quad (50)$$

where D^{MAC} represents a centered approximation to a cell-based divergence from edge-based velocities, and G^{MAC} represents a centered approximation to edge-based gradients from cell-centered data. The advective velocity is then

$$\mathbf{U}^{\text{ADV}} = \mathbf{U}^{\text{ADV},*} - \frac{1}{\rho^n} G^{\text{MAC}} \phi^{\text{MAC}} . \quad (51)$$

Step 3 *React the full state, then the base state, through the first time interval of $\Delta t/2$.*

- a. **React State** $(X_k^n, \rho^n, (\rho h)^n) \rightarrow (X_k^{(1)}, \rho^{(1)}, (\rho h)^{(1)}, (\rho \dot{w}_k)^{(1)})$.
- b. Define $(\overline{\rho \dot{w}_k})^{(1)} = \mathbf{Avg}(\rho \dot{w}_k)^{(1)}$.
- c. Define $(\overline{\rho H_{\text{ext}}})^{(1)} = \mathbf{Avg}(\rho^n H_{\text{ext}})$.
- d. **React Base** $((\rho X_k)_0^n, \rho_0^n, p_0^n, (\overline{\rho \dot{w}_k})^{(1)}, (\overline{\rho H_{\text{ext}}})^{(1)}) \rightarrow ((\rho X_k)_0^{(1)}, \rho_0^{(1)}, (\rho h)_0^{(1)}, p_0^{(1)}, \Gamma_{10}^{(1)}, \beta_0^{(1)})$.

Step 4 *Advect the base state, then the full state, through a time interval of Δt .*

- a. **Advect Base** $(\rho_0^{(1)}, p_0^{(1)}, (\rho X_k)_0^{(1)}, (\rho h)_0^{(1)}, \beta_0^{(1)}, w_0^{n+1/2,*}) \rightarrow (\rho_0^{(2),*}, p_0^{(2),*}, (\rho X_k)_0^{(2),*}, (\rho h)_0^{(2),*}, \beta_0^{(2),*})$
- b. Evolve $(\rho X_k)^{(1)} \rightarrow (\rho X_k)^{(2),*}$ and $(\rho h)^{(1)} \rightarrow (\rho h)^{(2),*}$ without explicitly including the reaction terms.

$$\begin{aligned} (\rho X_k)^{(2),*} &= (\rho X_k)^{(1)} + \left[(\rho X_k)_0^{(2),*} - (\rho X_k)_0^{(1)} \right] \\ &\quad - \Delta t \nabla \cdot \left\{ (\mathbf{U}^{\text{ADV}} + w_0^{n+1/2,*} \mathbf{e}_r) [(\rho X_k)']^{(1),n+1/2} \right\} \\ &\quad - \Delta t \nabla \cdot \left[(\rho X_k)_0^{(1)} \mathbf{U}^{\text{ADV}} \right] \end{aligned} \quad (52)$$

$$\begin{aligned} (\rho h)^{(2),*} &= (\rho h)^{(1)} + \left[(\rho h)_0^{(2),*} - (\rho h)_0^{(1)} \right] \\ &\quad - \Delta t \nabla \cdot \left\{ (\mathbf{U}^{\text{ADV}} + w_0^{n+1/2,*} \mathbf{e}_r) [(\rho h)']^{(1),n+1/2} \right\} \\ &\quad - \Delta t \nabla \cdot \left[(\rho h)_0^{(1)} \mathbf{U}^{\text{ADV}} \right] \\ &\quad + \frac{\Delta t}{2} w^{\text{ADV}} \left[\left(\frac{\partial p_0}{\partial r} \right)^{(1)} + \left(\frac{\partial p_0}{\partial r} \right)^{(2),*} \right] , \end{aligned} \quad (53)$$

$$\rho^{(2),*} = \sum_k (\rho X_k)^{(2),*} . \quad (54)$$

Then $X_k^{(2),*} = (\rho X_k)^{(2),*} / \rho^{(2),*}$.

Step 5 *React the full state, then the base state, through a second time interval of $\Delta t/2$.*

- a. **React State** $(X_k^{(2),*}, \rho^{(2),*}, (\rho h)^{(2),*}) \rightarrow (X_k^{n+1,*}, \rho^{n+1,*}, (\rho h)^{n+1,*}, (\rho \dot{w}_k)^{(2),*})$.
- b. Define $(\overline{\rho \dot{w}_k})^{(2),*} = \mathbf{Avg}(\rho \dot{w}_k)^{(2),*}$.
- c. Define $(\overline{\rho H_{\text{ext}}})^{(2),*} = \mathbf{Avg}(\rho^{(2),*} H_{\text{ext}})$.
- d. **React Base** $((\rho X_k)_0^{(2),*}, \rho_0^{(2),*}, p_0^{(2),*}, (\overline{\rho \dot{w}_k})^{(2),*}, (\overline{\rho H_{\text{ext}}})^{(2),*}) \rightarrow ((\rho X_k)_0^{n+1,*}, \rho_0^{n+1,*}, (\rho h)_0^{n+1,*}, p_0^{n+1,*}, \Gamma_{10}^{n+1,*}, \beta_0^{n+1,*})$.

Step 6 *Define a new average expansion rate at time $t^{n+1/2}$.*

- a. Define

$$S^{n+1,*} = -\sigma \sum_k (\xi_k + q_k) (\dot{w}_k)^{(2),*} + \frac{1}{\rho p_\rho} \sum_k p_{X_k} (\dot{w}_k)^{(2),*} + \sigma H_{\text{ext}} . \quad (55)$$

where $(\dot{w}_k)^{(2),*} = (\rho \dot{w}_k)^{(2),*} / \rho^{(2),*}$ and the remaining quantities are defined using $X_k^{n+1,*}$, $(\rho h)^{n+1,*}$, and $p_0^{n+1,*}$. Then define

$$S^{n+1/2} = \frac{1}{2}(S^n + S^{n+1,*}) .$$

- b. Define

$$\overline{S}^{n+1/2} = \mathbf{Avg}(S^{n+1/2}) .$$

- c. Define $w_0^{n+1/2}$ using $\overline{S}^{n+1/2}$ by solving equation (22) as described in Appendix B for spherical configurations, or by solving equation (21) for plane-parallel geometries. In the case of spherical geometries use $p_0^{n+1,*}$, $\Gamma_{10}^{n+1,*} = \Gamma_1(p_0^{n+1,*}, \rho_0^{n+1,*}, X_k^{n+1,*})$, and g as computed from $\rho_0^{n+1,*}$.

- d. Using equation (37), define

$$-\left(\frac{1}{\rho_0} \frac{\partial \pi_0}{\partial r}\right) = \frac{w_0^{n+1/2} - w_0^{n-1/2}}{\Delta t} + \left(w_0 \frac{\partial w_0}{\partial r}\right)^{n+1/2}$$

Step 7 *Repeat the construction of \mathbf{U}^{ADV} from Step 2 using updated quantities.*

Predict $\mathbf{U}^{\text{ADV},*}$ as in Step 2 but using $w_0^{n+1/2}$ instead of $w_0^{n+1/2,*}$ and π_0 from Step 6. Enforce the divergence constraint by solving

$$D^{\text{MAC}} \left(\frac{\beta_0^{n+1/2,*}}{\rho^{n+1/2,*}} G^{\text{MAC}} \phi^{\text{MAC}} \right) = D^{\text{MAC}} (\beta_0^{n+1/2,*} \mathbf{U}^{\text{ADV},*}) - \beta_0^{n+1/2,*} (S^{n+1/2} - \overline{S}^{n+1/2}) . \quad (56)$$

where $\rho^{n+1/2,\star} = 1/2(\rho^n + \rho^{n+1,\star})$ from Step 4 and $\beta_0^{n+1/2,\star} = 1/2(\beta_0^n + \beta_0^{n+1,\star})$ from Step 5. The advective velocity is then

$$\mathbf{U}^{\text{ADV}} = \mathbf{U}^{\text{ADV},\star} - \frac{1}{\rho^{n+1/2,\star}} G^{\text{MAC}} \phi^{\text{MAC}} . \quad (57)$$

Step 8 *Advect the base state, then the full state, through a time interval of Δt .*

- a. **Advect Base** $(\rho_0^{(1)}, p_0^{(1)}, (\rho X_k)_0^{(1)}, (\rho h)_0^{(1)}, \beta_0^{(1)}, w_0^{n+1/2}) \rightarrow (\rho_0^{(2)}, p_0^{(2)}, (\rho X_k)_0^{(2)}, (\rho h)_0^{(2)}, \beta_0^{(2)})$
- b. Evolve $(\rho X_k)^{(1)} \rightarrow (\rho X_k)^{(2)}$ and $(\rho h)^{(1)} \rightarrow (\rho h)^{(2)}$ as in Step 4 but using $w_0^{n+1/2}$ instead of $w_0^{n+1/2,\star}$.

Step 9 *React the full state, then the base state, through a second time interval of $\Delta t/2$.*

- a. **React State** $(X_k^{(2)}, \rho^{(2)}, (\rho h)^{(2)}) \rightarrow (X_k^{n+1}, \rho^{n+1}, (\rho h)^{n+1}, (\rho \dot{w}_k)^{(2)})$.
- b. Define $(\overline{\rho \dot{w}_k})^{(2)} = \mathbf{Avg}(\rho \dot{w}_k)^{(2)}$.
- c. Define $(\overline{\rho H_{\text{ext}}})^{(2)} = \mathbf{Avg}(\rho^{(2)} H_{\text{ext}})$.
- d. **React Base** $((\rho X_k)_0^{(2)}, \rho_0^{(2)}, p_0^{(2)}, (\overline{\rho \dot{w}_k})^{(2)}, (\overline{\rho H_{\text{ext}}})^{(2)}) \rightarrow ((\rho X_k)_0^{n+1}, \rho_0^{n+1}, (\rho h)_0^{n+1}, p_0^{n+1}, \Gamma_{10}^{n+1}, \beta_0^{n+1})$.

Step 10 *Compute S^{n+1} for the final projection.*

- a. Define
$$S^{n+1} = -\sigma \sum_k (\xi_k + q_k) (\dot{w}_k)^{(2)} + \frac{1}{\rho p_\rho} \sum_k p_{X_k} (\dot{w}_k)^{(2)} + \sigma H_{\text{ext}} , \quad (58)$$

where $(\dot{w}_k)^{(2)} = (\rho \dot{w}_k)^{(2)} / \rho^{(2)}$ and the remaining quantities are defined using X_k^{n+1} , $(\rho h)^{n+1}$, and p_0^{n+1} from Step 9.

- b. Define

$$\overline{S}^{n+1} = \mathbf{Avg}(S^{n+1}) .$$

Step 11 *Update the velocity.*

The velocity update happens analogously to paper II, using S^{n+1} from Step 10. We update the velocity field, $\tilde{\mathbf{U}}^n$ to $\tilde{\mathbf{U}}^{n+1,*}$ by discretizing equation (36),

$$\begin{aligned} \tilde{\mathbf{U}}^{n+1,*} &= \tilde{\mathbf{U}}^n - \Delta t (\mathbf{U}^{\text{ADV}} + w_0^{n+1/2} \mathbf{e}_r) \cdot \nabla \tilde{\mathbf{U}}^{n+1/2,*} - \Delta t (\mathbf{U}^{\text{ADV}} \cdot \mathbf{e}_r) \left(\frac{\partial w_0^{n+1/2}}{\partial r} \right) \mathbf{e}_r \\ &\quad + \Delta t \left[-\frac{1}{\rho^{n+1/2}} \nabla \pi^{n-1/2} + \left(\frac{1}{\rho_0} \nabla \pi_0 \right) - \frac{(\rho^{n+1/2} - \rho_0^{n+1/2})}{\rho^{n+1/2}} g \mathbf{e}_r \right], \end{aligned} \quad (59)$$

with $\tilde{\mathbf{U}}^{n+1/2,*}$ a velocity field extrapolated in time and space to edges, and $\rho^{n+1/2} = 1/2(\rho^n + \rho^{n+1})$. Details are given in paper II. Finally, we impose the constraint (Eq. [38])

$$\nabla \cdot (\beta_0^{n+1/2} \tilde{\mathbf{U}}^{n+1}) = \beta_0^{n+1/2} (S^{n+1} - \bar{S}^{n+1})$$

by solving

$$L_\beta^\rho \phi = D \left[\beta_0^{n+1/2} \left(\frac{\tilde{\mathbf{U}}^{n+1,*}}{\Delta t} + \frac{1}{\rho^{n+1/2}} \mathbf{G} \pi^{n-1/2} \right) \right] - \frac{1}{\Delta t} \beta_0^{n+1/2} (S^{n+1} - \bar{S}^{n+1})$$

for nodal values of ϕ where $\beta_0^{n+1/2} = 1/2(\beta_0^n + \beta_0^{n+1})$, L_β^ρ is the standard bilinear finite element approximation to $\nabla \cdot (\beta_0^{n+1/2} / \rho^{n+1/2}) \nabla$, and D and \mathbf{G} are discrete second-order operators that approximate the divergence and gradient, respectively. We determine the new-time velocity field from

$$\tilde{\mathbf{U}}^{n+1} = \tilde{\mathbf{U}}^{n+1,*} - \frac{\Delta t}{\rho^{n+1/2}} (\mathbf{G} \phi - \mathbf{G} \pi^{n-1/2}),$$

and the new time-centered perturbational pressure from

$$\pi^{n+1/2} = \phi.$$

Step 12 *Compute a new Δt .*

Compute Δt for the next time step with the procedure described in § 3.4, using w_0 as computed in Step 6 and $\tilde{\mathbf{U}}^{n+1}$ as computed in Step 11. We will use this Δt in the next time step.

This completes the time advancement of the algorithm.

3.3. Initialization

While (ρX_k) , (ρh) , $(\rho X_k)_0$, and $(\rho h)_0$ are specified by the user at the beginning of the evolution, it is not trivial to specify an initial velocity field that satisfies an initial approximation to the divergence constraint. We use an iterative procedure to compute both an

initial right-hand-side for the constraint equation and an initial velocity field that satisfies the constraint. The user specifies the number of iterations, N_{iters}^S , in this first step of the initialization procedure.

The initial perturbational pressure also needs to be determined, for use in Steps 2, 7 and 11. This is done through a second iterative procedure which follows the time-advancement algorithm as described in steps 1-11 in the previous subsection. The user specifies the number of iterations, N_{iters}^π , in this second step of the initialization procedure. The details for both iterations are given below.

Step 0 Initialization

Start with initial data, $X_k^{\text{init}}, \rho^{\text{init}}$, and $(\rho h)^{\text{init}}$ and the base state, and an initial guess for the velocity, \mathbf{U}^{init} . Set $\mathbf{U}^1 = \mathbf{U}^{\text{init}}$ and $w_0^1 = 0$ as an initial approximation. Compute β_0^{init} as a function of the initial data. The first part of the initialization process proceeds as follows.

- a. **do** $\nu = 1, \dots, N_{iters}^S$
 - i. Estimate Δt^ν using \mathbf{U}^ν and w_0^ν .
 - ii. **React State** $(X_k^{\text{init}}, \rho^{\text{init}}, (\rho h)^{\text{init}}) \rightarrow (X_k^{\text{out}}, \rho^{\text{out}}, (\rho h)^{\text{out}}, (\rho \dot{w}_k)^{0,\nu})$.
 - iii. Compute $S^{0,\nu}$ from equation (15) using $(\rho \dot{w}_k)^{0,\nu}$ and the initial data.
 - iv. Compute $\bar{S}^{0,\nu} = \mathbf{Avg}(S^{0,\nu})$.
 - v. Compute $w_0^{\nu+1}$ as in Step 1c using $\bar{S}^{0,\nu}$ and the initial data.
 - vi. Project \mathbf{U}^ν using β_0^{init} and $(S^{0,\nu} - \bar{S}^{0,\nu})$ as the source term. This yields $\mathbf{U}^{\nu+1}$.

end do

Define $S^0 = S^{0,N_{iters}^S}$ and $\Delta t = \Delta t^{N_{iters}^S}$.

Next, we need to construct an approximation to the time-centered perturbational pressure, π , and an approximation to the divergence constraint at the end of the first time step. Let $S^{1,0} = S^0$ as an initial approximation, and define, as a first approximation, $\pi^{-1/2} = 0$.

- b. **do** $\nu = 0, \dots, N_{iters}^\pi - 1$

- i. Perform Steps 1–11 as described above, using $S^{1/2,*} = \frac{1}{2}(S^0 + S^{1,\nu})$ in Step 1 as described. These steps yield new scalar and velocity data at time Δt , which we discard. They also yield new values for $S^{1,\nu+1}$ (Step 10) and $\pi^{1/2}$ (Step 11), which we keep.

ii. Set $\pi^{-1/2} = \pi^{1/2}$

end do

Define $S^1 = S^{1, N_{\text{iters}}^\pi}$.

Once we have defined S^0 and S^1 , we can use the extrapolation procedure described in Step 1 of the algorithm to predict the time-centered $S^{n+1/2}$ needed in the subsequent steps. Finally, we define $w_0^{-1/2} = 0$.

3.4. Computing the Time Step

There are several constraints on the time step; effectively we compute the time step based on each constraint separately, then take the minimum value of the various time steps computed.

The first set of constraints is based on the standard CFL condition for explicit methods. The user sets a CFL factor, σ^{CFL} , between 0 and 1. Because we advance the base state with w_0 only, and the full state with $(\mathbf{U} + w_0 \mathbf{e}_r)$, we have two separate constraints based on the CFL condition. For a calculation in n_{dim} dimensions ($n_{\text{dim}} = 2$ or 3), the first constraint is

$$\Delta t_{\mathbf{U}} = \sigma^{\text{CFL}} \min_{i=1 \dots n_{\text{dim}}} \{\Delta t_i\} \quad (60)$$

where

$$\Delta t_i = \min_{\mathbf{x}} \left\{ \frac{\Delta x_i}{\left| \tilde{U}_i + w_0^{\text{cell}} \mathbf{e}_r \cdot \mathbf{n}_i \right|} \right\} \quad (61)$$

Here w_0^{cell} is the value of w_0 averaged from the cell edges to each cell center, \mathbf{n}_i is the normal in the i^{th} coordinate direction and $\min_{\mathbf{x}}$ is the minimum taken over all computational grid cells in the domain.

The second constraint is based entirely on w_0 :

$$\Delta t_{w_0} = \sigma^{\text{CFL}} \min_j \left\{ \frac{\Delta r}{|w_{0j}|} \right\} \quad (62)$$

where Δr is the spacing of the radial arrays such as the base state and w_{0j} is the value of w_0 at a radius of $j\Delta r$. For plane parallel simulations $\Delta r = \Delta x$, but in the spherical simulations Δr and Δx need not be the same.

An additional constraint is based on the forcing terms rather than the velocities. This constraint is necessary when a calculation is started from rest, since in that case the velocity-based time step would be infinite.

Here, we define

$$\Delta t_F = \min_{i=1\dots n_{\text{dim}}} \{\Delta t_{F_i}\} \quad (63)$$

where

$$\Delta t_{F_i} = \sqrt{2\Delta x_i / F_{i_{\text{max}}}} \quad (64)$$

where $F_{i_{\text{max}}}$ is the maximum buoyancy force in the i^{th} coordinate direction.

A final time step constraint is needed to prevent local expansion from numerically emptying a cell. We require that the density be reduced by no more than 40% in a single time step; this is expressed in terms of constraining the time step so that $\Delta t \leq \Delta t_S$, where Δt_S is defined at the beginning of each time step so that

$$\Delta t_S (\nabla \cdot \tilde{\mathbf{U}}^n) \leq 0.40$$

in every cell.

For the initial iterations described in the initialization section above, none of these methods may give a reasonable time step if there is no initial velocity field. In that case, we set the time step to the fully compressible time step constraint—i.e. that determined by the bulk velocity plus sound speed.

4. Numerical Results

In this section we present results exploring different features of the low Mach number algorithm in a plane-parallel geometry. The first set of simulations are bubble rise problems with reactions. We compare the low Mach number results with compressible results, and also perform a convergence study of the low Mach number method. The second set of simulations are of long-timescale convection; again we compare with compressible results, and in addition examine the long-time behavior of the thermodynamic pressure relative to the background pressure to verify that the model assumptions continue to hold. All of these tests are performed with the general astrophysical equation of state (Timmes & Swesty 2000), suitable to the conditions in a white dwarf.

4.1. Background State

For each of our numerical tests we define the background state in three parts, as in paper II. The central portion of the domain is initialized with a one-dimensional hydrostatic white dwarf model. The model is created by specifying a base density of $2.6 \times 10^9 \text{ g cm}^{-3}$ and base temperature of $7 \times 10^8 \text{ K}$ and integrating the equation of hydrostatic equilibrium outward while constraining the model to be isentropic. The composition is held constant at 0.3 ^{12}C and 0.7 ^{16}O , and the gravitational acceleration is fixed at $-1.5 \times 10^{10} \text{ cm s}^{-2}$. This procedure provides a reasonable approximation of the state of the white dwarf just before runaway.

Below this layer, we decrease the entropy by a factor of 3 and create a convectively stable layer by integrating downward with a constant entropy gradient, so that the entropy decreases slowly towards the bottom of the domain. This layer acts as part of the lower boundary condition to insulate the dynamics in the unstable layer from the effects of the lower boundary of the computational domain. The entropy drop here is large enough that the temperatures in this layer are $< 10^7 \text{ K}$, and the thermonuclear reactions are effectively turned off.

The upper portion of the domain represents the region beyond the outer boundary of the white dwarf, and different approximations are used there for the compressible and low Mach number models. For the compressible calculations, the integration proceeds radially outward until the density reaches a threshold value of $10^{-4} \text{ g cm}^{-3}$. Throughout the integration, however, the temperature is never allowed to drop below 10^7 K . Once the density drops below its cutoff, the integration is stopped and the material above it is held at constant density and temperature. Figure 1 of paper II shows the initial temperature, density, entropy, and adiabatic indices (Γ_1 and $\gamma_e \equiv p/(\rho e) + 1$) as a function of height for the compressible background.

For the low Mach number model the density cutoff is set to $3 \times 10^6 \text{ g cm}^{-3}$. Once the density reaches this cutoff the density, temperature and pressure are held constant, equivalent to gravity being set to zero radially outward of that position. The motivation for this cutoff is discussed in paper II. An additional approximation we use in the outer region is to define β_0 by keeping β_0/ρ_0 constant for $\rho_0 < 5 \times 10^7 \text{ g cm}^{-3}$ in order to suppress spurious wave formation at the outer boundary of the star. We refer to the radius at which $\rho_0 = 5 \times 10^7 \text{ g cm}^{-3}$ as the “anelastic cutoff.”

4.2. Reacting Bubble Rise

To test the coupling of reactions to the hydrodynamics, we consider a plane-parallel carbon/oxygen white dwarf model seeded with temperature perturbations. For these calculations we restrict ourselves to a plane-parallel geometry in order to test the reactions separately from the geometry and to more easily facilitate the comparisons to a fully compressible code.

We use a single-step $^{12}\text{C}(^{12}\text{C}, \gamma)^{24}\text{Mg}$ reaction. The carbon mass fraction equation appears as:

$$\frac{DX(^{12}\text{C})}{Dt} = -\frac{1}{12}\rho X(^{12}\text{C})^2 f_{\text{Coul}} [N_A \langle \sigma v \rangle] \quad (65)$$

where $N_A \langle \sigma v \rangle$ is evaluated using the reaction rate from Caughlan & Fowler (1988). The Coulomb screening factor, f_{Coul} , is evaluated using the general routine from the Kepler stellar evolution code (Weaver et al. 1978), which implements the work of Graboske et al. (1973) for weak screening and Alastuey & Jancovici (1978); Itoh et al. (1979) for strong screening. Larger networks can easily be accommodated.

The initial conditions for the two bubble rise problems are defined to be the background state, as defined in § 4.1, perturbed by the addition of local temperature variations (with corresponding density perturbations that keep the perturbed regions in pressure equilibrium with the background) of the form:

$$\begin{aligned} T_{i,j} &= T_{0j} \left\{ 1 + \sum_{m=1}^3 a_m \left[1 + \tanh \left(2 - \frac{d_m}{\sigma_m} \right) \right] \right\} \\ \rho_{i,j} &= \rho(p_{0j}, T_{i,j}, X_{k0,j}) \end{aligned} \quad (66)$$

Here, i and j are the lateral and vertical zone indices respectively, T_{0j} and p_{0j} are the base state temperature and pressure, and $X_{k0,j}$ is the base state mass fraction of species k . The distance d_m is simply found as $d_m^2 = (x_i - x_m)^2 + (r_j - r_m)^2$. No explicit heating source term is included—these perturbations are large enough to begin localized carbon burning in the model star. In addition to the burning in the rising bubbles, the conditions at the base of our convectively unstable layer (where $\rho = 2 \times 10^9 \text{ g cm}^{-3}$ and $T = 7 \times 10^8 \text{ K}$), which correspond to those at the center of a white dwarf a short time before an SNe Ia, are such that low level reactions also occur here.

4.2.1. Comparison with Compressible

This first test is similar to that presented in paper II, except now the heating is provided by reactions. For this test we use 3 perturbations, whose coordinates x_m and r_m , width σ_m , and amplitude a_m are listed in Table 1. We compare the low Mach number results with both an unsplit and dimensionally split implementation of the compressible upwind method of Colella (1990).

The domain is $2.16 \times 10^8 \text{ cm} \times 3.6 \times 10^8 \text{ cm}$, of which the bottom $0.5 \times 10^8 \text{ cm}$ is the low entropy layer. The resolution is 384×640 cells. Periodic boundary conditions are used on the left and right domain edges. The low Mach number runs use a solid wall boundary at the lower boundary and outflow at the upper boundary. The fully compressible simulations use a hydrostatic lower boundary and a zero-gradient upper boundary.

Figure 1 shows the temperature (calculated from the equation of state given enthalpy, density and composition) and ^{24}Mg abundance after 2.5 s of evolution, for the split and unsplit compressible algorithms and the low Mach algorithm. Generally, the results agree well between the algorithms. As discussed in papers I and II, the bubbles in the low Mach number case are slightly narrower than those from the compressible runs, but as we showed there, the magnitude of the disparity is comparable to that between different compressible algorithms. We note that the dimensionally split compressible algorithm used in this paper is different algorithm than the split algorithm used in papers I and II. With this new algorithm, we do not see the temperature oscillations that we attributed to dimensional splitting in paper I.

Another feature of the algorithm that we explore with this simulation is the effect of replacing Γ_1 by Γ_{10} in the definition of α (Eq. [9]). We consider equation (8) in the form

$$\nabla \cdot \mathbf{U} + \frac{1}{\Gamma_1 p_0} \frac{Dp_0}{Dt} = S \text{ .}$$

We argued in paper I that we could replace Γ_1 in the above equation by Γ_{10} , allowing us to write equation (8) in the form of equation (10). Instead, we could substitute a more general expression, $\Gamma_1 = \Gamma_{10} + \delta\Gamma_1$, into equation (8), giving

$$\nabla \cdot \mathbf{U} + \frac{1}{(\Gamma_{10} + \delta\Gamma_1) p_0} \mathbf{U} \cdot \nabla p_0 = S - \frac{1}{(\Gamma_{10} + \delta\Gamma_1) p_0} \frac{\partial p_0}{\partial t} \text{ .}$$

Most of the influence of a varying Γ_1 enters through the $\mathbf{U} \cdot \nabla p_0$ term, so we neglect the $\delta\Gamma_1$ contribution to the base state expansion term. Assuming that $\delta\Gamma_1 \ll \Gamma_{10}$, we then have

$$\nabla \cdot \mathbf{U} + \frac{1}{\Gamma_{10} p_0} \mathbf{U} \cdot \nabla p_0 = S - \frac{1}{\Gamma_{10} p_0} \frac{\partial p_0}{\partial t} + \frac{\delta\Gamma_1}{\Gamma_{10}^2 p_0} \mathbf{U} \cdot \nabla p_0 \text{ ,}$$

which can be written as

$$\nabla \cdot (\beta_0 \mathbf{U}) = \beta_0 \left(S - \frac{1}{\Gamma_{10} p_0} \frac{\partial p_0}{\partial t} + \frac{\delta \Gamma_1}{\Gamma_{10}^2 p_0} \mathbf{U} \cdot \nabla p_0 \right) . \quad (67)$$

After decomposing the velocity field, this would yield the equation,

$$\nabla \cdot (\beta_0 \tilde{\mathbf{U}}) = \beta_0 \left(S - \bar{S} + \frac{\delta \Gamma_1}{\Gamma_{10}^2 p_0} \tilde{\mathbf{U}} \cdot \nabla p_0 \right) , \quad (68)$$

instead of equation (38). In order to solve this equation using the projection methodology, we consider a time-lagged approximation to the $\tilde{\mathbf{U}} \cdot \nabla p_0$ term appearing on the right hand side. We explore the effect of substituting equation (68) for equation (38) in both the MAC projection (Steps 2 and 7) and the final projection (Step 11).

Figure 2 shows a superposition of contours of the temperature from the original simulation (using just Γ_{10} in equation (8)) and the temperature from the same simulation except using the $\delta \Gamma_1$ correction in the projections. We see that there is very little difference in the two temperature fields, supporting our original substitution of Γ_{10} for Γ_1 in the velocity constraint equation.

4.2.2. Convergence Study

In the calculations considered here we zoom in on a single reacting bubble. The domain spans only 1.44×10^8 cm in the horizontal and vertical directions, of which the bottom 0.1×10^8 cm is the low entropy layer. We initialize one hot spot in the form of equation (66), centered laterally in the domain at elevation $r = r_2$ with $\sigma = \sigma_2$ and $a = a_2$, as given in Table 1. The calculations are run with a fixed time step to $t = 1.0$ s, and data is presented at intervals of 0.2 s. The time steps for the coarse, medium and fine resolutions are $\Delta t = 0.02$ s, 0.01 s, and 0.005 s, respectively. The resolutions are $\Delta r = 1125000$ cm, 562500 cm, and 281250 cm, respectively. The boundary conditions are solid wall on the lower boundary, periodic on the lateral boundaries, and outflow at the upper boundary.

To compute rates of convergence, we first compute the errors between data differing by a factor of two in resolution. The error is defined at the coarser of the two resolutions by the difference between the coarser calculation and the volumetrically-averaged finer calculation of each set. The L_1 norm of each error is then computed, and the ratio of the coarse-medium error to the medium-fine error is computed and presented in the table. Ratios of approximately 4 denote second-order convergence.

For these simulations, the sharpness of the transition at the artificial low entropy layer at the bottom of the domain introduces errors at the interface that obscure the convergence

behavior of the scheme. In addition, we want to focus on the bubble dynamics rather than the upper atmosphere where the flow is smoother. For these reasons, we measure errors in a subset of the domain, from 0.27×10^8 cm to 0.81×10^8 cm in the vertical direction. Figure 3 shows the temperature field at $t = 1$ s in the region of interest.

In Table 3 we present the ratios of the L_1 norms of the errors in velocity, perturbational density and temperature, enthalpy, and ^{24}Mg abundance. At early times, the data shows second-order behavior for all of the primary variables. At intermediate times, we begin to see a reduced convergence rate $\approx h^{1.6}$ in the ^{24}Mg abundance. We believe that this reduced rate results from the extreme sensitivity of the reaction rate to temperature, $O(T^{23})$ (Woosley et al. 2004). At later times, we see this reduction in the convergence rate appearing in the perturbational temperature and density fields.

Another important test of the behavior of the methodology is the degree to which the solution drifts from the equation of state, i.e. the degree to which the thermodynamic pressure, defined by the equation of state as a function of density, enthalpy and composition, differs from p_0 over time. This drift occurs because the algorithm enforces the Lagrangian derivative of the equation of state through the divergence constraint on velocity, but does not strictly enforce the equation of state itself at each time step. Consequently, although $p(\rho, h, X_k) \equiv p_0$ at initial time, this equality is not strictly maintained over time.

In this calculation, in addition to measuring the difference between coarse and fine solutions, we monitor two quantities that reflect this drift. The first is $(\delta p)_{\text{drift}} = |p(\rho, h, X_k) - p_0|$, the second is $(\delta T)_{\text{drift}} = |T_\rho - T_h|$, where T_ρ is defined from the equation of state using p_0, ρ , and X_k , and T_h is defined from ρ, h , and X_k .

In Table 4 we present the convergence rates of $(\delta p)_{\text{drift}}/p_0$ and $(\delta T)_{\text{drift}}$. We note that the magnitude of $(\delta p)_{\text{drift}}$ never exceeds 0.01% of p_0 at any point in the region of interest. Furthermore, the magnitude of $(\delta T)_{\text{drift}}$ never exceeds 1% of T_h . In addition, we see from Table 4 that both of these quantities show strict second-order convergence. (We note that no values are shown for $t = 0.0$ in Table 4 because $(\delta p)_{\text{drift}}$ and $(\delta T)_{\text{drift}}$ are identically zero there at all resolutions.)

4.3. Plane Parallel Convection

In this section we consider longer-time convection in our model atmosphere, again in a plane-parallel geometry for the purpose of easier comparison between the compressible and low Mach number algorithms. In order to allow for better control over the heating that drives the convection, we use a prescribed heating rate, specified through H_{ext} as defined in

the above algorithm.

For the tests presented in this section, we use a heating term of the form

$$H_{\text{ext},j} = H_0 \exp \left\{ -(r_j - r_{\text{layer}})^2 / W^2 \right\} \left[1 + \sum_{m=1}^{n_{\text{pert}}} b_m \sin \left(\frac{k_m \pi x_i}{L_x} + \Psi_m \right) \right] \quad (69)$$

Here, H_0 is the absolute heating rate (to be specified below), r_{layer} is the height at which the heating is centered, and L_x is the width of the domain. The amplitudes, b_m , modes, k_m , and phases, Ψ_m , of the sinusoidal perturbations are listed in Table 2.

4.3.1. *Sponge Layer*

The large drop in density at the surface of the star results in high velocities in the region above the surface when high heating rates are used in a plane-parallel geometry. This region should not affect the dynamics below the surface in the convecting regions of the star. However, because the time step in the low Mach number code is limited by the highest velocity in the computational domain, the efficiency gains of the low Mach number algorithm are reduced if those velocities persist.

To address this we employ a damping technique commonly used in modeling atmospheric convection (see, for example Durran (1990)). A forcing term is added to the velocity update before the final projection at the end of each time step in the form

$$\mathbf{U}^{\text{new}} = \mathbf{U}^{\text{old}} - \Delta t \kappa f_{\text{damp}} \mathbf{U}^{\text{new}} .$$

We note that solving this implicitly for \mathbf{U}^{new} is equivalent to multiplying \mathbf{U}^{old} by the factor $1/(1 + \Delta t \kappa f_{\text{damp}})$ to define \mathbf{U}^{new} .

The sponge profile, f_{damp} , takes the form

$$f_{\text{damp}} = \begin{cases} 0 & \text{if } z < z_{\text{sp}} \\ \frac{1}{2} \left\{ 1 - \cos \left[\pi \left(\frac{z - z_{\text{sp}}}{z_{\text{tp}} - z_{\text{sp}}} \right) \right] \right\} & \text{if } z_{\text{sp}} \leq z < z_{\text{tp}} \\ 1 & \text{if } z \geq z_{\text{tp}} \end{cases} \quad (70)$$

Here, z_{sp} is the height above which the damping term becomes nonzero, and z_{tp} is the height at which the forcing reaches its maximum. We can think of $1/\kappa$ as the timescale over which we want to drive the velocities back to zero. Since the background profiles are allowed to shift, we define the location of the sponge dynamically in terms of the background density.

For the low Mach number algorithm we simply multiply $\tilde{\mathbf{U}}^{*,n+1}$ in Step 11 by the factor above before solving the elliptic equation to impose the divergence constraint. In the compressible algorithm, the velocity is multiplied by this factor at the end of each time step.

In the next subsection, we explore the effect of the damping by contrasting compressible calculations with and without the sponge layer as well as the low Mach number calculation with a sponge layer.

4.3.2. Convection Example: Comparison with Compressible

The first convection problem we consider is run with 320×512 cells in a domain of 2.5×10^8 cm \times 4.0×10^8 cm, of which the bottom 10^8 cm is the low entropy layer. We note that this layer is thicker than that used in the bubble rise simulations, because we wish to further insulate the convection from the effects of the lower boundary. For the sponge layer $\kappa = 100$ s $^{-1}$. The average time step in the low Mach calculations is $\overline{\Delta t} \sim 10^{-3}$ s, so our choice of κ means that the velocities in the sponge layer will be damped over $(1/\kappa)/\overline{\Delta t} \sim 10$ time steps. In order to compare our low Mach number results with those from the compressible algorithm, for these simulations we fix the sponge transition heights at $z_{\text{sp}} = 2.19140625 \times 10^8$ cm and $z_{\text{tp}} = 2.97265625 \times 10^8$ cm. As with the bubble rise calculations, the lateral boundary conditions are periodic. In the compressible simulations, the upper boundary is zero-gradient and the lower boundary is hydrostatic, while in the low Mach number simulation the lower boundary is solid wall while the upper boundary is outflow.

For the heating we choose $r_{\text{layer}} = 1.25 \times 10^8$ cm (i.e. just 250 km above the base of our convectively unstable layer), and $W = 10^7$ cm. For this example, we include only the first three perturbational modes ($n_{\text{pert}} = 3$) from Table 2. We want to choose H_0 large enough that the compressible algorithm can be used for comparison, but not so large that we exceed the limits of validity of the low Mach number approach. We find that $H_0 = 2.5 \times 10^{16}$ erg g $^{-1}$ s $^{-1}$ results in a Mach number that remains below 0.4 in the atmosphere. For reference, the thermonuclear energy generation rate at the base of the convectively unstable layer (away from the perturbations) in the previous test was $\sim 3 \times 10^{13}$ erg g $^{-1}$ s $^{-1}$, very close to the analytic estimate provided by Woosley et al. (2004) for our base conditions ($\rho = 2 \times 10^9$ g cm $^{-3}$ and $T = 7 \times 10^8$ K). Since our choice of H_0 is much higher than the energy generation rate we would expect during the smoldering phase of SNe Ia evolution, we expect this to be a very demanding test of the low Mach algorithm.

Figure 4 shows the temperature field after 5 seconds and after 10 seconds for the low

Mach number algorithm, and for the compressible algorithm with and without the sponge layer. We consider a region of interest, which we will define as $10^8 \text{ cm} \leq r \leq 2.2 \times 10^8 \text{ cm}$ —i.e. the domain excluding the low entropy region at the bottom and sponge layer at the top. In the region of interest we see good qualitative agreement in the overall features of the solution in all three cases; however, because of the highly unstable character of convection over long times we do not expect point-by-point agreement. A more appropriate comparison is to examine the overall statistics of the convective flow. Here, since we are not including reactions we focus on the average and RMS fluctuations of temperature. In particular, we define the lateral average of T ,

$$\langle T \rangle_j = \frac{1}{N_x} \sum_{i=1}^{N_x} T_{i,j} , \quad (71)$$

where N_x is the number of cells in the lateral direction and the RMS fluctuations

$$(\delta T)_j = \left[\frac{1}{N_x} \sum_{i=1}^{N_x} (T_{i,j} - \langle T \rangle_j)^2 \right]^{1/2} . \quad (72)$$

Figure 5 shows both the average and deviation of the temperature at both times. First, we examine the difference between the compressible solution with and without the sponge layer. At both 5 and 10 s, we see very strong agreement between these two runs in the region of interest. While the solutions differ both above and below the region of interest, this result gives us confidence in the location and strength of the sponge layer.

Next we compare the compressible and low Mach solutions. Again, the solutions agree very well in the region of interest. In the low entropy layer below the region of interest, we do see noticeable differences between the solutions; however these deviations are small in magnitude and do not appear to affect the solution in the region of interest. (We attribute the low Mach number results to the small vortices penetrating the low entropy layer from above, as seen in Figure 4. We suspect the presence of these vortices is due to the reflecting wall boundary condition at the lower boundary.)

For this calculation, we note that the magnitude of $(\delta p)_{\text{drift}}/p_0$ never exceeds 1.0% in the convectively unstable region below the sponge layer.

4.3.3. Convection Example: Long-Time Study

In our final simulation, we reduce the magnitude of the heating and simulate for a longer time. The domain for this simulation is $5 \times 10^8 \text{ cm} \times 3.5 \times 10^8 \text{ cm}$, of which the bottom $0.5 \times 10^8 \text{ cm}$ is the low entropy layer. We use 640×448 cells, and follow the large-scale

convection to $t = 60$ s. The location of the sponge is adjusted dynamically as discussed in Section 4.3.1. In particular, we define the middle of the transition region, $z_{\text{md}} = 1/2(z_{\text{tp}} + z_{\text{sp}})$, to be the location of the density cutoff, i.e., where ρ_0 reaches $3.0 \times 10^6 \text{ g cm}^{-3}$. We define z_{hw} as the location where $\rho_0 = 10^7 \text{ g cm}^{-3}$. Then $z_{\text{sp}} = z_{\text{md}} - 2(z_{\text{md}} - z_{\text{hw}})$, and $z_{\text{tp}} = z_{\text{md}} + 2(z_{\text{md}} - z_{\text{hw}})$. The heating is again in the form of equation (69) with $r_{\text{layer}} = 7.5 \times 10^7 \text{ cm}$, $W = 10^7 \text{ cm}$, and $H_0 = 1.0 \times 10^{14}$. Here we use four perturbational modes ($n_{\text{pert}} = 4$), with the amplitudes, b_m , modes, k_m , and phases, Ψ_m , of the sinusoidal perturbations given in Table 2.

Figure 6 shows a time sequence of temperature and vorticity from this calculation in the lower $2.5 \times 10^8 \text{ cm}$ of the domain. In this example, the early time dynamics shows the emergence of large-scale regular structures in the principal region of interest with some small scale mixing at the boundary of the low entropy region. At $t = 20\text{s}$ we begin to see the breakdown into smaller structures. At later times the temperature shows a large-scale layered structure with small scale perturbations while the vorticity shows that the flow is now dominated by small-scale mixing. For this simulation, the sponge effectively suppresses unphysical high velocities above the anelastic cutoff. Examination of the Mach number shows that the Mach number remains below 0.09 for the entire simulation, so that at this reduced heating the flow remains in the low Mach number regime.

Figure 7 shows the magnitude of $(\delta p)_{\text{drift}}/p_0$. For this calculation, we also note that this never exceeds 1.0% in the convectively unstable region below the sponge layer, in spite of the long-time integration.

5. Conclusions

This paper is the third in a set of three papers that has demonstrated a new algorithm for evolving low Mach number reacting flows in Type Ia supernovae. In paper I, we demonstrated the accuracy of the low Mach number approach for non-reacting flows, with no base state adjustment, in a stellar atmosphere. In paper II, we extended the methodology to allow for time evolution of the base state in response to significant heating. Finally, in this paper, we have extended the algorithm to incorporate nuclear chemistry characteristic of the early stages of SNe Ia. The simulation code described here, named **MAESTRO**, will be our primary tool for exploring the conditions leading up to the explosion of Type Ia supernovae.

We have demonstrated that in the presence of reactions that we can attain second order accuracy in the thermodynamic variables. We further demonstrated that our method remains stable over long timescale evolution of fully convective flow in plane-parallel geometry and

that the thermodynamic pressure calculated from the equation of state does in fact remain close to the time-dependent background pressure. Finally, we have motivated the changes necessary to model a self-gravitating star and showed that we can again successfully capture the expansion of the background state in response to heating in a spherical geometry.

Throughout the development of this new algorithm, we have validated the new methodology with detailed comparisons to fully compressible codes. Due to their wide availability and ease of implementation, compressible algorithms are the current workhorse of multidimensional stellar astrophysics. We have shown that the low Mach number algorithm remains stable and captures the essential features of the flow even for Mach numbers in excess of 0.2. Although the low Mach number algorithm is more complicated than compressible algorithms, it reduces the number of time steps needed to reach a particular time by a factor of $\sim 1/M$ relative to compressible codes.

Our next step in the development of this methodology will be to complete the implementation in three dimensions and address the remaining numerical issues needed to model a spherical star in Cartesian geometry. Further improvements include adaptive mesh refinement and more sophisticated reaction networks. Ultimately, we will augment the present algorithm with methodology for capturing long wavelength acoustics in order to be able to evolve the flow from the very subsonic regime through Mach numbers close to unity.

We thank Alan Calder, Jonathan Dursi, Gary Glatzmaier, and Stan Woosley for helpful comments on this manuscript. This work was supported by the SciDAC Program of the DOE Office of Mathematics, Information, and Computational Sciences under the U.S. Department of Energy under contract No. DE-AC02-05CH11231 and by a DOE/Office of Nuclear Physics Outstanding Junior Investigator award, grant No. DE-FG02-06ER41448, to SUNY Stony Brook. The compressible calculations presented here used portions of the FLASH Code (version 2.5), developed in part by the DOE-supported ASC/Alliance Center for Astrophysical Thermonuclear Flashes at the University of Chicago.

A. Evaluating ξ_k and p_{X_k}

Adding the reactions to the equation set brings with it two additional thermodynamic quantities that we need to evaluate:

$$\xi_k = \left. \frac{\partial h}{\partial X_k} \right|_{p,T,(X_j,j \neq k)} ; \quad p_{X_k} = \left. \frac{\partial p}{\partial X_k} \right|_{\rho,T,(X_j,j \neq k)} .$$

In evaluating these expressions, it is important to note what is being held constant. The stellar equation of state we use (Timmes & Swesty (2000)) is a function of ρ , T , \bar{A} , and \bar{Z} , where the latter two variables are composition terms:

$$\bar{A} \equiv \left(\sum_k \frac{X_k}{A_k} \right)^{-1} ; \quad \bar{Z} \equiv \bar{A} \sum_k \frac{Z_k X_k}{A_k} ,$$

where A_k is the atomic mass of species k , and Z_k is the charge. The thermodynamic derivatives returned by the equation of state routine are with respect to one of these variables while holding the others fixed. Therefore, we want to express these quantities in terms of derivatives with respect to ρ , T , \bar{A} , and \bar{Z} . This means that we need to find an alternate expression for ξ_k , so that ρ and T are held constant, rather than p and T , and we need to express both ξ_k and p_{X_k} as derivatives with respect to \bar{A} and \bar{Z} .

In deriving the temperature equation, equation (7), we started with the enthalpy, which is the most natural thermodynamic quantity when pressure is one of the independent variables. Here, we want ρ to be an independent variable, so starting with the internal energy, e , is more natural. The internal energy evolution of the system is governed by

$$\rho \frac{De}{Dt} + p \nabla \cdot \mathbf{U} = - \sum_k \rho q_k \dot{\omega}_k$$

or, using the mass continuity equation,

$$\rho \frac{De}{Dt} = \frac{p}{\rho} \frac{D\rho}{Dt} - \sum_k \rho q_k \dot{\omega}_k \tag{A1}$$

Now, taking $e = e(\rho, T, X_k)$, we have

$$\frac{De}{Dt} = \left. \frac{\partial e}{\partial T} \right|_{\rho, X_k} \frac{DT}{Dt} + \left. \frac{\partial e}{\partial \rho} \right|_{T, X_k} \frac{D\rho}{Dt} + \sum_k \left. \frac{\partial e}{\partial X_k} \right|_{\rho, T, (X_j, j \neq k)} \frac{DX_k}{Dt}$$

Identifying the specific heat at constant volume as $c_v = \partial e / \partial T|_{\rho, X_k}$, defining $e_\rho \equiv \partial e / \partial \rho|_{T, X_k}$ and $e_{X_k} \equiv \partial e / \partial X_k|_{\rho, T, (X_j, j \neq k)}$, and using the species conservation equation, this is

$$\frac{De}{Dt} = c_v \frac{DT}{Dt} + e_\rho \frac{D\rho}{Dt} + \sum_k e_{X_k} \dot{\omega}_k$$

Substituting this into equation (A1), we have

$$\rho c_v \frac{DT}{Dt} = \rho \left(\frac{p}{\rho^2} - e_\rho \right) \frac{D\rho}{Dt} - \sum_k \rho e_{X_k} \dot{\omega}_k - \sum_k \rho q_k \dot{\omega}_k$$

We can eliminate $D\rho/Dt$ using equation (6), giving

$$\begin{aligned} \rho \left[c_v + \left(\frac{p}{\rho^2} - e_\rho \right) \frac{p_T}{p_\rho} \right] \frac{DT}{Dt} = \\ \frac{\rho}{p_\rho} \left(\frac{p}{\rho^2} - e_\rho \right) \frac{Dp}{Dt} - \sum_k \rho \left[e_{X_k} + \frac{1}{p_\rho} \left(\frac{p}{\rho^2} - e_\rho \right) p_{X_k} \right] \dot{\omega}_k - \sum_k \rho q_k \dot{\omega}_k \quad (\text{A2}) \end{aligned}$$

Comparing to equation (7), we see that the specific heats are related via

$$c_p = c_v + \left(\frac{p}{\rho^2} - e_\rho \right) \frac{p_T}{p_\rho}$$

The coefficient of the Dp/Dt term gives

$$h_p = \frac{1}{\rho} \left(1 - \frac{p}{\rho p_\rho} \right) + \frac{1}{p_\rho} e_\rho$$

which was used in paper I when computing α . Finally, we have

$$\xi_k = e_{X_k} + \frac{1}{p_\rho} \left(\frac{p}{\rho^2} - e_\rho \right) p_{X_k} \quad (\text{A3})$$

where all the derivatives on the right hand side are either at constant T or constant ρ . This is the form we will need when computing ξ_k from our equation of state.

As discussed in Dursi & Timmes (2006), we can evaluate the derivatives with respect to the species from the average compositional variables \bar{A} and \bar{Z} , using the chain rule, as the equation of state routine does when it returns derivatives with respect to \bar{A} and \bar{Z} . We write e_{X_k} and p_{X_k} as

$$\begin{aligned} p_{X_k} &= \left. \frac{\partial p}{\partial \bar{A}} \right|_{\rho, T, \bar{Z}} \frac{\partial \bar{A}}{\partial X_k} + \left. \frac{\partial p}{\partial \bar{Z}} \right|_{\rho, T, \bar{A}} \frac{\partial \bar{Z}}{\partial X_k} \\ &= -\frac{\bar{A}^2}{A_k} \left. \frac{\partial p}{\partial \bar{A}} \right|_{\rho, T, \bar{Z}} + \frac{\bar{A}}{A_k} (Z_k - \bar{Z}) \left. \frac{\partial p}{\partial \bar{Z}} \right|_{\rho, T, \bar{A}} \quad (\text{A4}) \end{aligned}$$

$$\begin{aligned} e_{X_k} &= \left. \frac{\partial e}{\partial \bar{A}} \right|_{\rho, T, \bar{Z}} \frac{\partial \bar{A}}{\partial X_k} + \left. \frac{\partial e}{\partial \bar{Z}} \right|_{\rho, T, \bar{A}} \frac{\partial \bar{Z}}{\partial X_k} \\ &= -\frac{\bar{A}^2}{A_k} \left. \frac{\partial e}{\partial \bar{A}} \right|_{\rho, T, \bar{Z}} + \frac{\bar{A}}{A_k} (Z_k - \bar{Z}) \left. \frac{\partial e}{\partial \bar{Z}} \right|_{\rho, T, \bar{A}} \quad (\text{A5}) \end{aligned}$$

Then ξ_k can be evaluated from equation (A3).

B. Modifications for a Spherical Self-Gravitating Star

In paper II, we calculated the hydrostatic expansion of the base state in plane-parallel geometry under the assumption that the weight of the material above (or below) any given fluid parcel does not change during hydrostatic expansion. This assumption holds when the gravitational acceleration is independent of location. Here we discuss the modifications to the present algorithm required to treat a spherical self-gravitating star.

B.1. Calculation of w_0

In the low Mach number model, we allow the density and temperature perturbations to be large compared to the background state, but we require the pressure perturbation to be small. Therefore, if the star expands, we need to incorporate that expansion into the background state. Furthermore, we need to know the velocity of the base state expansion for the evolution of the perturbed quantities.

We begin with equation (19) written in spherical coordinates

$$\frac{1}{r^2} \frac{\partial}{\partial r} (r^2 \beta_0 w_0) = \beta_0 \left(\bar{S} - \frac{1}{\Gamma_1 p_0} \frac{\partial p_0}{\partial t} \right)$$

and expand the spatial derivative and divide through by β_0 .

$$\frac{1}{r^2} \frac{\partial}{\partial r} (r^2 w_0) + w_0 \frac{1}{\beta_0} \frac{\partial \beta_0}{\partial r} = \left(\bar{S} - \frac{1}{\Gamma_1 p_0} \frac{\partial p_0}{\partial t} \right). \quad (\text{B1})$$

Recalling from paper I that

$$\frac{1}{\Gamma_1 p_0} \frac{\partial p_0}{\partial r} = \frac{1}{\beta_0} \frac{\partial \beta_0}{\partial r}$$

we can express equation (B1) as

$$\begin{aligned} \frac{1}{r^2} \frac{\partial}{\partial r} (r^2 w_0) + w_0 \frac{1}{\Gamma_1 p_0} \frac{\partial p_0}{\partial r} &= \left(\bar{S} - \frac{1}{\Gamma_1 p_0} \frac{\partial p_0}{\partial t} \right) \\ \frac{1}{r^2} \frac{\partial}{\partial r} (r^2 w_0) &= \bar{S} - \frac{1}{\Gamma_1 p_0} \left(\frac{\partial p_0}{\partial t} + w_0 \frac{\partial p_0}{\partial r} \right) \end{aligned} \quad (\text{B2})$$

Multiplying equation (B2) through by $\Gamma_1 p_0$, taking another derivative with respect to r , and switching the order of temporal and spatial derivatives, we get

$$\frac{\partial}{\partial r} \left[\frac{\Gamma_1 p_0}{r^2} \frac{\partial}{\partial r} (r^2 w_0) \right] = \frac{\partial (\Gamma_1 p_0 \bar{S})}{\partial r} - \frac{\partial}{\partial t} \frac{\partial p_0}{\partial r} - \frac{\partial}{\partial r} \left(w_0 \frac{\partial p_0}{\partial r} \right) \quad (\text{B3})$$

For the case of non-constant gravity in a spherical geometry, the equation of hydrostatic equilibrium is

$$\frac{\partial p_0}{\partial r} = -\rho_0(r)g(r); \quad g(r) = \frac{Gm(r)}{r^2}$$

where $m(r)$ is the mass enclosed at radius r and G is the gravitational constant. Using this, we can then write equation (B3) as

$$\begin{aligned} \frac{\partial}{\partial r} \left[\frac{\Gamma_1 p_0}{r^2} \frac{\partial}{\partial r} (r^2 w_0) \right] &= \frac{\partial(\Gamma_1 p_0 \bar{S})}{\partial r} + \frac{\partial}{\partial t} [\rho_0 g(r)] + \frac{\partial}{\partial r} [w_0 \rho_0 g(r)] \\ &= \frac{\partial(\Gamma_1 p_0 \bar{S})}{\partial r} + g(r) \left[\frac{\partial \rho_0}{\partial t} + \frac{\partial}{\partial r} (w_0 \rho_0) \right] + \rho_0 \left(\frac{\partial g}{\partial t} + w_0 \frac{\partial g}{\partial r} \right) \end{aligned} \quad (\text{B4})$$

We can utilize the fact that as the star expands, the Lagrangian derivative of the mass enclosed does not change,

$$\frac{Dm}{Dt} = 0$$

which allows us to write the Lagrangian change in the gravitational acceleration as

$$\frac{\partial g}{\partial t} + w_0 \frac{\partial g}{\partial r} = \frac{Dg}{Dt} = -2 \frac{Gm}{r^3} \frac{Dr}{Dt} = -2 \frac{Gm w_0}{r^3} = -2 \frac{w_0 g}{r}$$

Putting it all together, equation (B4) becomes

$$\frac{\partial}{\partial r} \left[\frac{\Gamma_1 p_0}{r^2} \frac{\partial}{\partial r} (r^2 w_0) \right] = \frac{\partial(\Gamma_1 p_0 \bar{S})}{\partial r} + g(r) \left[\frac{\partial \rho_0}{\partial t} + \frac{\partial}{\partial r} (w_0 \rho_0) \right] + \rho_0 \left(\frac{-2w_0 g}{r} \right)$$

Finally, we can use conservation of mass,

$$\frac{\partial \rho_0}{\partial t} + \frac{1}{r^2} \frac{\partial (r^2 \rho_0 w_0)}{\partial r} = 0 \quad (\text{B5})$$

to write this as

$$\begin{aligned} \frac{\partial}{\partial r} \left[\frac{\Gamma_1 p_0}{r^2} \frac{\partial}{\partial r} (r^2 w_0) \right] &= \frac{\partial(\Gamma_1 p_0 \bar{S})}{\partial r} + g(r) \left[-\frac{1}{r^2} \frac{\partial}{\partial r} (r^2 w_0 \rho_0) + \frac{\partial}{\partial r} (w_0 \rho_0) \right] + \rho_0 \left(\frac{-2w_0 g}{r} \right) \\ &= \frac{\partial(\Gamma_1 p_0 \bar{S})}{\partial r} - \frac{4w_0 \rho_0 g}{r} \end{aligned} \quad (\text{B6})$$

This elliptic equation is much more complicated than that derived in paper II for plane-parallel atmospheres. We discretize this in one dimension as

$$\frac{1}{\Delta r} \left\{ \left[\frac{\Gamma_1 p_0}{r^2} \frac{\partial (r^2 w_0)}{\partial r} \right]_i - \left[\frac{\Gamma_1 p_0}{r^2} \frac{\partial (r^2 w_0)}{\partial r} \right]_{i-1} \right\} = \frac{1}{\Delta r} \left[(\Gamma_1 p_0 \bar{S})_i - (\Gamma_1 p_0 \bar{S})_{i-1} \right] - 4 \left[\frac{w_0 \rho_0 g(r)}{r} \right]_{i-1/2}$$

which expands to

$$\frac{1}{\Delta r} \left\{ \left(\frac{\Gamma_1 p_0}{r^2} \right)_i \frac{[(r^2 w_0)_{i+1/2} - (r^2 w_0)_{i-1/2}]}{\Delta r} - \left(\frac{\Gamma_1 p_0}{r^2} \right)_{i-1} \frac{[(r^2 w_0)_{i-1/2} - (r^2 w_0)_{i-3/2}]}{\Delta r} \right\} = \frac{(\Gamma_1 p_0 \bar{S})_i - (\Gamma_1 p_0 \bar{S})_{i-1}}{\Delta r} - 4 \left[\frac{\rho_0 g(r)}{r} \right]_{i-1/2} (w_0)_{i-1/2} \quad (\text{B7})$$

If we write this in matrix form, so that

$$A_i (w_0)_{i-3/2} + B_i (w_0)_{i-1/2} + C_i (w_0)_{i+1/2} = F_i \quad (\text{B8})$$

then

$$A_i = \frac{1}{\Delta r^2} \left(\frac{\Gamma_1 p_0}{r^2} \right)_{i-1} (r^2)_{i-3/2} \quad (\text{B9a})$$

$$B_i = -\frac{1}{\Delta r^2} \left[\left(\frac{\Gamma_1 p_0}{r^2} \right)_i + \left(\frac{\Gamma_1 p_0}{r^2} \right)_{i-1} \right] (r^2)_{i-1/2} + 4 \left(\frac{\rho_0 g}{r} \right)_{i-1/2} \quad (\text{B9b})$$

$$C_i = \frac{1}{\Delta r^2} \left(\frac{\Gamma_1 p_0}{r^2} \right)_i (r^2)_{i+1/2} \quad (\text{B9c})$$

$$F_i = \frac{(\Gamma_1 p_0 \bar{S})_i - (\Gamma_1 p_0 \bar{S})_{i-1}}{\Delta r} \quad (\text{B9d})$$

Here

$$g_{i-1/2} = \frac{G}{r_{i-1/2}^2} \sum_{k=1}^i \frac{4}{3} \pi (r_{k-1/2}^3 - r_{k-3/2}^3) \rho_{0k-1} \quad (\text{B10})$$

We define the lower boundary condition, $w = 0$ at $r = 0$, which corresponds to $i = 1$, by setting

$$\begin{aligned} A_1 = C_1 = F_1 &= 0 \\ B_1 &= 1 \end{aligned}$$

We also specify $w = 0$ at the the upper boundary, which corresponds to $i = N$, by setting

$$\begin{aligned} A_N &= 0 \\ B_N &= 1 \\ C_N = F_N &= 0 \end{aligned}$$

B.2. React Base

The **React Base** step for the spherical self-gravitating star is identical to that for the plane-parallel constant gravity case. However, in the self-gravitating case one must

recompute gravity after each call to **React Base** because gravity is used to define the new β_0 .

B.3. Advect Base

1. Species and Density Update:

The species update now includes the area factors in the divergences:

$$(\rho X_k)_{0,j}^{\text{out}} = (\rho X_k)_{0,j}^{\text{in}} - \frac{1}{r_j^2} \frac{\Delta t}{\Delta r} \left\{ [r^2 (\rho X_k)_0^{\text{in}, n+1/2} w_0^{\text{in}}]_{j+1/2} - [r^2 (\rho X_k)_0^{\text{in}, n+1/2} w_0^{\text{in}}]_{j-1/2} \right\} \quad (\text{B11})$$

As before, the interface states are found via the procedure described in paper II, Appendix A. The base state density is again simply

$$\rho_0^{\text{out}} = \sum_k (\rho X_k)_0^{\text{out}} .$$

With the new density distribution, we can compute the new gravitational acceleration for the spherical case, $g^{\text{out}} = g(\rho_0^{\text{out}})$, using using equation (B10).

2. Pressure Update:

We use a predictor-corrector formulation for the pressure update in order to gain second-order accuracy. First, we discretize the left hand side of equation (28) by time-centering the pressure evolution as

$$\frac{1}{\Gamma_{10} p_0} \frac{\partial p_0}{\partial t} \approx \frac{2}{\Gamma_{10}^{\text{in}} (p_0^{\text{in}} + p_0^*)} \frac{p_0^* - p_0^{\text{in}}}{\Delta t}$$

We can then solve for the provisional updated pressure, p_0^* , giving

$$p_0^* = p_0^{\text{in}} \frac{1 + \Gamma_{10}^{\text{in}} f}{1 - \Gamma_{10}^{\text{in}} f} \quad (\text{B12})$$

with

$$f = \frac{\Delta t}{2} \left\{ \bar{S}^{\text{in}} - \left[\frac{1}{\beta_0^{\text{in}}} \nabla \cdot (\beta_0^{\text{in}} w_0^{\text{in}} \mathbf{e}_r) \right] \right\}$$

Now we begin the corrector step. Using the equation of state, we compute

$$\Gamma_{10}^* = \Gamma_1(\rho_0^{\text{out}}, p_0^*, X_k^{\text{out}}) .$$

We then use this to construct

$$\beta_0^\star = \beta_0(g^{\text{out}}, \Gamma_{10}^\star, p_0^\star) \ .$$

A time-centered approximation to β_0 can now be computed:

$$\tilde{\beta}_0 = \frac{1}{2}(\beta_0^{\text{in}} + \beta_0^\star)$$

This allows us to complete the corrector for the pressure update

$$p_0^{\text{out}} = p_0^{\text{in}} \frac{1 + \Gamma_{10}^{\text{in}} \tilde{f}}{1 - \Gamma_{10}^\star \tilde{f}} \quad (\text{B13})$$

with

$$\tilde{f} = \frac{\Delta t}{2} \left\{ \tilde{S}^{\text{in}} - \left[\frac{1}{\tilde{\beta}_0} \nabla \cdot (\tilde{\beta}_0 w_0^{\text{in}} \mathbf{e}_r) \right] \right\}$$

3. Enthalpy Update:

After the base state species and pressure are updated, we compute the updated base state enthalpy,

$$(\rho h)_{0,j}^{\text{out}} = (\rho h)_{0,j}^{\text{in}} - \frac{1}{r_j^2} \frac{\Delta t}{\Delta r} \left\{ [r^2(\rho h)_0^{\text{in}, n+1/2} w_0^{\text{in}}]_{j+1/2} - [r^2(\rho h)_0^{\text{in}, n+1/2} w_0^{\text{in}}]_{j-1/2} \right\} + \Delta t \eta \quad (\text{B14})$$

in the spherical case, where η is found by discretizing equation (29). This update is a discretization over an interval of Δt of

$$\frac{\partial(\rho h)_0}{\partial t} = -\nabla \cdot [(\rho h)_0 w_0] + \eta \ ,$$

i.e., equation (30) without the terms due to heating but including η . Finally, using the equation of state, we now compute

$$\Gamma_{10}^{\text{out}} = \Gamma_1(\rho_0^{\text{out}}, p_0^{\text{out}}, X_{k0}^{\text{out}}) \ ,$$

and use this to construct

$$\beta_0^{\text{out}} = \beta_0(\rho_0^{\text{out}}, \Gamma_{10}^{\text{out}}, p_0^{\text{out}}) \ .$$

B.4. One-dimensional Results

To test the spherical base state expansions, we inject heat at a steady rate into a one-dimensional white dwarf model. This is similar to the first test in paper II, except now in spherical coordinates. As in that test, the compressible method with which we compare the low Mach number method is the FLASH (Fryxell et al. 2000) code’s implementation of the piecewise-parabolic method (PPM) (Colella & Woodward 1984) in a one-dimensional spherical geometry. The initial conditions for the white dwarf are those described in § 4.1 for the central region.

In the expansion of a plane-parallel atmosphere, heating at a height r above the base does not affect the pressure or density below that height. By contrast, in a spherical symmetric self-gravitating star, heating at a radius r will lead to a pressure and density decrease at the center in addition to the expansion of the outer layers (Schwarzschild & Härm 1965).

We apply a heating function of the form

$$H_{\text{ext}} = H_0 \exp \left[-(r - r_0)^2 / W^2 \right] \quad , \quad (\text{B15})$$

with $r_0 = 4 \times 10^7$ cm, $W = 10^7$ cm, and $H_0 = 1 \times 10^{16}$ erg g^{−1} s^{−1}. This is the same functional form as used in the first test of paper II, but with a lower amplitude. Still, this heating rate is far higher than what is expected during the convective phase of Type Ia SNe. The heating term is added to the enthalpy equation in the low Mach number equations in the same fashion as described in paper II. In this test, we do not consider reactions. Since this is a one-dimensional test all perturbational quantities, as well as $\tilde{\mathbf{U}}$, are zero, so we are directly testing the computation of w_0 as described in Appendix B, and the base state update as described in the **Advect Base** procedure defined above. Both the PPM and low Mach calculation use 768 zones in a domain 5×10^8 cm high.

Figure 8 shows the structure of the star after heating for 10 s. The gray line is the initial star before any heating. We see that the compressible and low Mach number models agree extremely well. Both capture the decrease in the density and pressure at the center of the star and the considerable expansion in radius. Only at the surface of the star do the temperatures differ slightly. In all calculations, we set the minimum temperature to 5×10^6 K. The PPM simulation required 13488 steps and the low Mach (CFL = 0.5) calculation needed 203. Over the course of the simulation, the Mach number of the flow remained less than 0.35, with the maximum Mach number occurring at the surface of the star. This Mach number pushes the limits of validity of the low Mach number model; a smaller perturbation amplitude would result in a smaller Mach number.

C. Computing β_0

A high-order reconstruction of the integrand in the β_0 integral (Eq. [11]) improves the overall solution relative to a lower-order reconstruction. Here we outline the integration procedure using piecewise linear reconstruction of the state variables. We wish to compute

$$\beta_0(r, t) = \beta_0(0, t) \exp \left(\int_0^r \frac{1}{(\Gamma_1 p)_0} \frac{\partial p_0}{\partial r'} dr' \right) .$$

We split the integral such that we integrate from the low edge of each cell to the high edge, resulting in edge-centered values of β_0 . The initial value of β_0 on the lowest edge of the domain will be assigned the value $\beta_{01/2} = \rho_{01}$. Letting i be the index in the radial direction, we define β_0 on the high edge of cell i using

$$\beta_{0i+1/2} = \beta_{01/2} \exp \left[- \sum_{j=1}^i \int_{r_{j-1/2}}^{r_{j+1/2}} \frac{\rho_0(r') |g(r')|}{\Gamma_{10}(r') p_0(r')} dr' \right] = \beta_{01/2} \prod_{j=1}^i \exp \left[- \int_{r_{j-1/2}}^{r_{j+1/2}} \frac{\rho_0(r') |g(r')|}{\Gamma_{10}(r') p_0(r')} dr' \right]$$

Beginning with $\beta_{01/2}$, we integrate over the first cell ($i = 1$) to define $\beta_{03/2}$, and continue integrating cell-by-cell. We use piecewise linear reconstruction of ρ_0 , Γ_{10} , p_0 :

$$\begin{aligned} \rho_0(r) &= \rho_{0j} + \lambda_j(r - r_j) , \\ \Gamma_{10}(r) &= \Gamma_{10j} + \mu_j(r - r_j) , \\ p_0(r) &= p_{0j} + \nu_j(r - r_j) . \end{aligned}$$

Here, the average value of each quantity is just the zonal value and the slopes (λ , μ , and ν) are computed simply as centered differences, for example,

$$\lambda_j = \frac{\rho_{0j+1} - \rho_{0j-1}}{2\Delta r} .$$

We can now compute the integral

$$I_j \equiv |g(r_j)| \int_{r_j - \Delta r/2}^{r_j + \Delta r/2} \frac{\rho_0(r')}{\Gamma_{10}(r') p_0(r')} dr' = |g(r_j)| \int_{r_j - \Delta r/2}^{r_j + \Delta r/2} \frac{\rho_{0j} + \lambda_j(r' - r_j)}{[\Gamma_{10j} + \mu_j(r' - r_j)] [p_{0j} + \nu_j(r' - r_j)]} dr' .$$

Substituting $\eta = \rho_{0j} + \lambda_j(r - r_j)$, we have

$$I_j = \frac{|g(r_j)|}{\lambda_j} \int_{\rho_{0j} - \lambda_j \Delta r/2}^{\rho_{0j} + \lambda_j \Delta r/2} \frac{\eta d\eta}{(\Gamma_{10j} - \rho_{0j} \mu_j / \lambda_j + \mu_j \eta / \lambda_j) (p_{0j} - \rho_{0j} \nu_j / \lambda_j + \nu_j \eta / \lambda_j)} .$$

Using a table of integrals, this evaluates to

$$I_j = \frac{|g(r_j)|}{\nu_j \Gamma_{10j} - \mu_j p_{0j}} \left[\left(\frac{\lambda_j \Gamma_{10j}}{\mu_j} - \rho_{0j} \right) \ln \left(\frac{\Gamma_{10j} + \mu_j \Delta r/2}{\Gamma_{10j} - \mu_j \Delta r/2} \right) - \left(\frac{\lambda_j p_{0j}}{\nu_j} - \rho_{0j} \right) \ln \left(\frac{p_{0j} + \nu_j \Delta r/2}{p_{0j} - \nu_j \Delta r/2} \right) \right] . \quad (C1)$$

The interface values of β_0 are then evaluated as

$$\beta_{0_{i+1/2}} = \rho_0 \prod_{j=1}^i \exp\{-I_j\} \ .$$

Cell-centered values of β_0 are found by simple averaging,

$$\beta_{0_i} = \frac{1}{2} (\beta_{0_{i-1/2}} + \beta_{0_{i+1/2}}) \ .$$

REFERENCES

- Alastuey, A., & Jancovici, B. 1978, *ApJ*, 226, 1034
- Almgren, A. 2000, *Journal of Atmospheric Sciences*, 57, 995
- Almgren, A. S., Bell, J. B., Colella, P., Howell, L. H., & Welcome, M. 1998, *Journal of Computational Physics*, 142, 1
- Almgren, A. S., Bell, J. B., Rendleman, C. A., & Zingale, M. 2006a, *ApJ*, 637, 922, paper I
- . 2006b, *ApJ*, 649, 927, paper II
- Baraffe, I., Heger, A., & Woosley, S. E. 2004, *ApJ*, 615, 378
- Bell, J. B., Day, M. S., Rendleman, C. A., Woosley, S. E., & Zingale, M. A. 2004, *Journal of Computational Physics*, 195, 677
- Bell, J. B., & Marcus, D. L. 1992, *Journal of Computational Physics*, 101, 334
- Brown, P. N., Byrne, G. D., & Hindmarsh, A. C. 1989, *SIAM J. Sci. Stat. Comput.*, 10, 1038
- Caughlan, G. R., & Fowler, W. A. 1988, *Atomic Data and Nuclear Data Tables*, 40, 283, see also <http://www.phy.ornl.gov/astrophysics/data/cf88/index.html>
- Colella, P. 1990, *Journal of Computational Physics*, 87, 171
- Colella, P., & Woodward, P. R. 1984, *Journal of Computational Physics*, 54, 174
- Durran, D. 1990, *Meteorol. Monographs*, 23, 59
- Dursi, L. J., & Timmes, F. X. 2006, *ApJ*, 641, 1071
- Fryxell, B. et al. 2000, *Astrophysical Journal Supplement*, 131, 273
- García-Senz, D., & Bravo, E. 2005, *A&A*, 430, 585
- Graboske, H. C., Dewitt, H. E., Grossman, A. S., & Cooper, M. S. 1973, *ApJ*, 181, 457
- Höflich, P., & Stein, J. 2002, *Astrophysical Journal*, 568, 779
- Hillebrandt, W., & Niemeyer, J. C. 2000, *Annu. Rev. Astron. Astrophys.*, 38, 191
- Itoh, N., Totsuji, H., Ichimaru, S., & Dewitt, H. E. 1979, *ApJ*, 234, 1079
- Kuhlen, M., Woosley, S. E., & Glatzmaier, G. A. 2006, *Astrophysical Journal*, 640, 407

- Lin, D. J., Bayliss, A., & Taam, R. E. 2006, ArXiv Astrophysics e-prints
- Livne, E., Asida, S. M., & Höflich, P. 2005, ApJ, 632, 443
- Nicoud, F. 2000, Journal of Computational Physics, 158, 71
- Niemeyer, J. C., Hillebrandt, W., & Woosley, S. E. 1996, ApJ, 471, 903
- Plewa, T., Calder, A. C., & Lamb, D. Q. 2004, Astrophysical Journal, 612, L37
- Röpke, F. K., Hillebrandt, W., Niemeyer, J. C., & Woosley, S. E. 2006a, A&A, 448, 1
- Röpke, F. K., Woosley, S. E., & Hillebrandt, W. 2006b, ArXiv Astrophysics e-prints
- Schwarzschild, M., & Härm, R. 1965, ApJ, 142, 855
- Sussman, M. M., Almgren, A. S., Bell, J. B., Colella, P., Howell, L., & Welcome, M. 1999, Journal of Computational Physics, 148, 81
- Timmes, F. X., & Swesty, F. D. 2000, ApJS, 126, 501
- Weaver, T. A., Zimmerman, G. B., & Woosley, S. E. 1978, Astrophysical Journal, 225, 1021
- Woosley, S. E., Wunsch, S., & Kuhlen, M. 2004, Astrophysical Journal, 607, 921
- Wunsch, S., & Woosley, S. E. 2004, ApJ, 616, 1102

Table 1: Parameters for initial temperature perturbations (see Eq. [66]).

m	a_m	x_m (cm)	r_m (cm)	σ_m (cm)
1	0.15	5.0×10^7	6.5×10^7	2.5×10^6
2	0.30	1.2×10^8	8.5×10^7	2.5×10^6
3	0.225	2.0×10^8	7.5×10^7	2.5×10^6

Table 2: Parameters for heating rates (see Eq. [69].)

m	b_m	k_m	Ψ_m
1	0.00625	2	0
2	0.01875	6	$\pi/3$
3	0.01250	8	$\pi/5$
4	0.00250	1	0.562

Table 3: Ratios of L_1 errors of dynamic and thermodynamic variables.

	$t = 0.0$	$t = 0.2$	$t = 0.4$	$t = 0.6$	$t = 0.8$	$t = 1.0$
u	4.2	3.7	3.4	3.3	3.3	3.5
v	4.0	3.9	3.7	3.6	3.7	3.7
$X(^{24}\text{Mg})$		4.3	3.8	2.9	3.1	3.0
$\rho - \rho_0$	4.0	3.8	3.6	3.8	3.6	3.0
$T - T_0$	4.0	3.8	3.7	3.8	3.6	2.9
h	4.0	4.0	4.0	4.0	4.0	3.9

Table 4: Ratios of L_1 errors of $(\delta p)_{\text{drift}}$ and $(\delta T)_{\text{drift}}$.

	$t = 0.2$	$t = 0.4$	$t = 0.6$	$t = 0.8$	$t = 1.0$
$(\delta p)_{\text{drift}}$	3.8	3.8	3.9	3.9	4.0
$(\delta T)_{\text{drift}}$	3.8	3.8	3.9	3.9	4.0

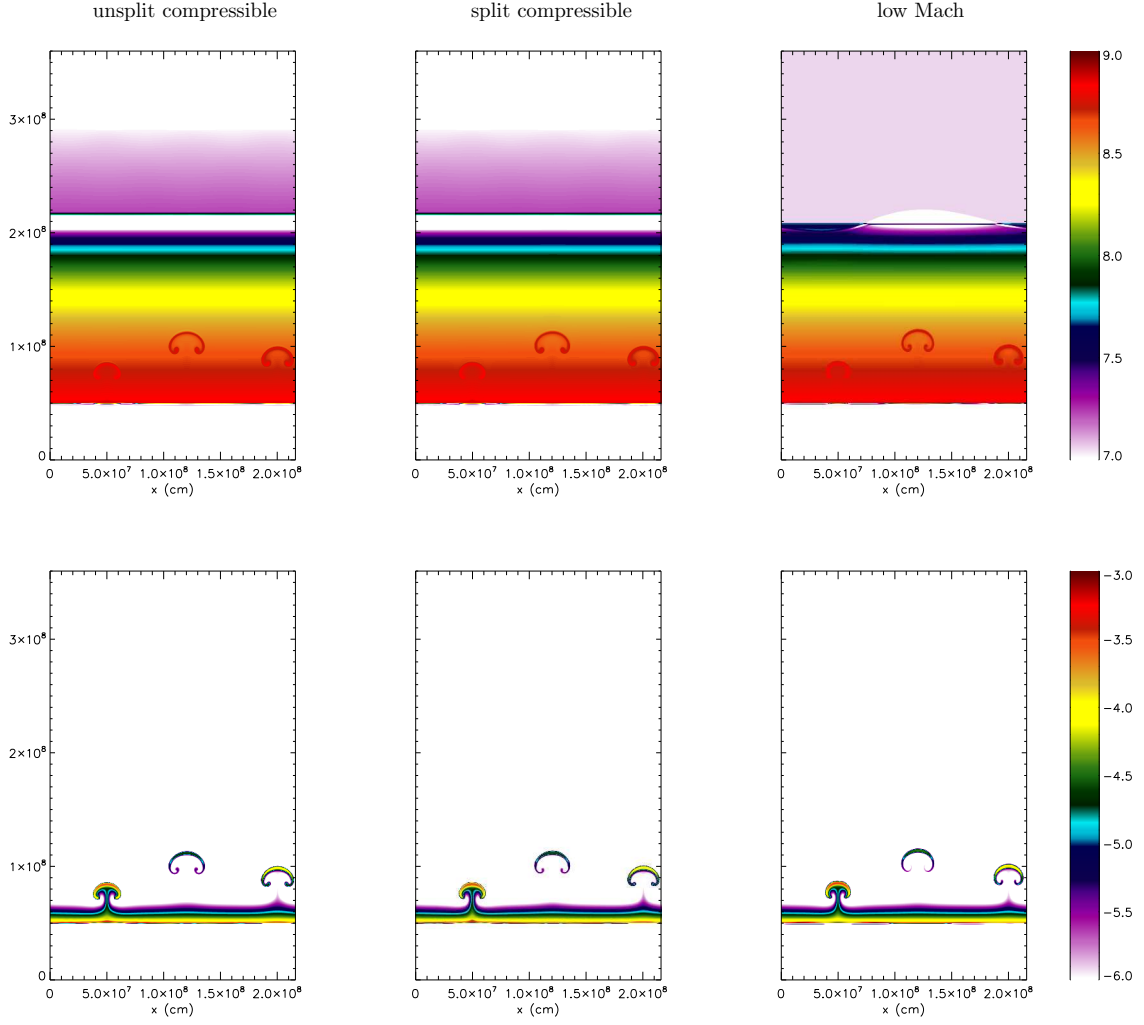


Fig. 1.— Comparison of the low Mach (left) and compressible (right) solutions for the three-bubble test. Shown are the temperature (top row) and ^{24}Mg mass fraction (bottom row) at $t = 2.5$ s.

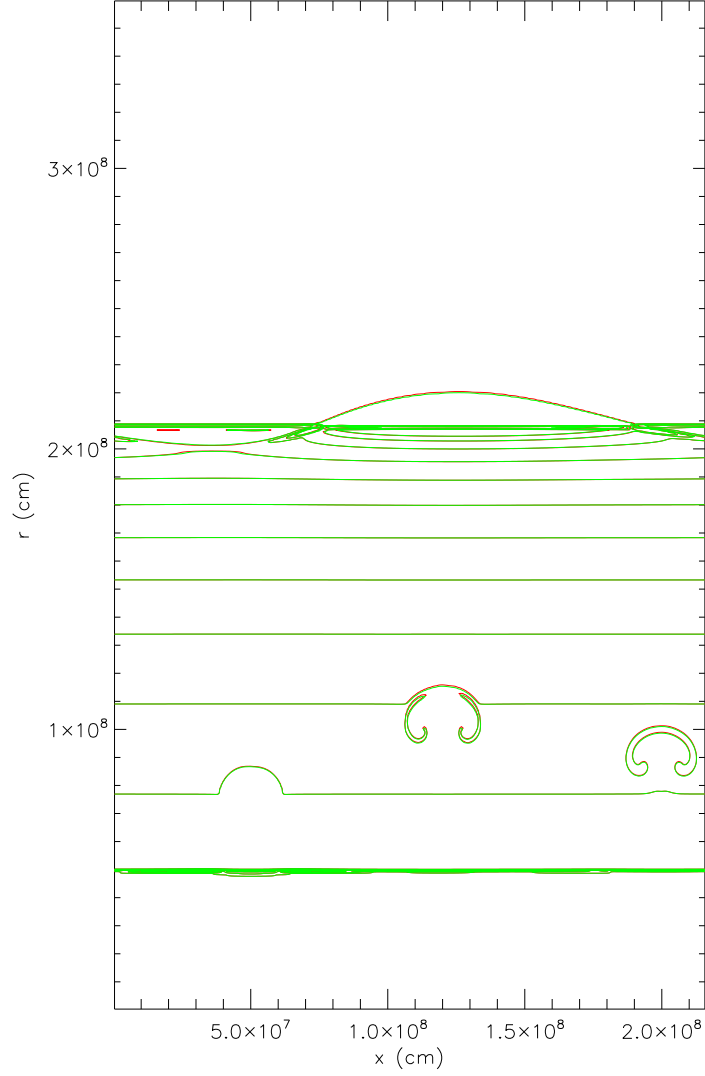


Fig. 2.— Comparison of the effect of using only Γ_{10} (red) vs. the lagged $\delta\Gamma_1$ correction (green). Here, the temperature is plotted, with 12 contours equally spaced in $\log T$ in the range $10^7 \text{ K} \leq T \leq 8 \times 10^8 \text{ K}$. We see excellent agreement between the simulations, demonstrating that it is reasonable to use only Γ_{10} in equation (9).

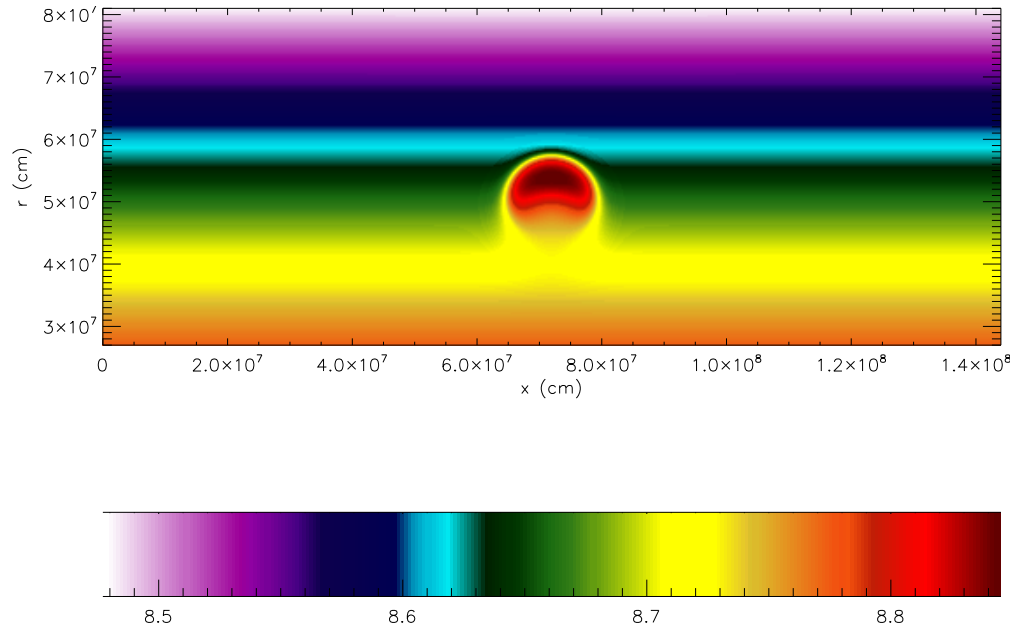


Fig. 3.— Temperature at $t = 1$ s in the region of interest of the bubble rise problem used for the convergence study.

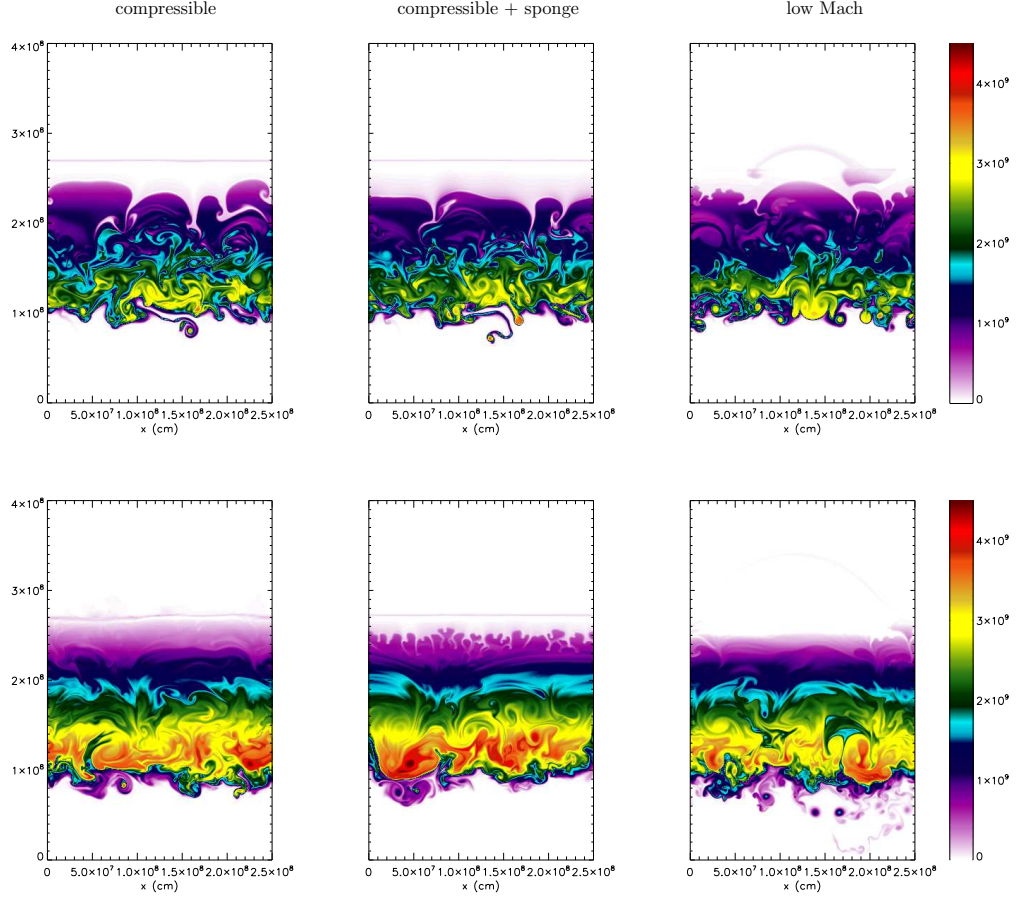


Fig. 4.— Temperature at $t = 5$ s and $t = 10$ s in the first convection example. Shown are results using the compressible algorithm with and without a sponge layer, and the low Mach number algorithm with a sponge layer.

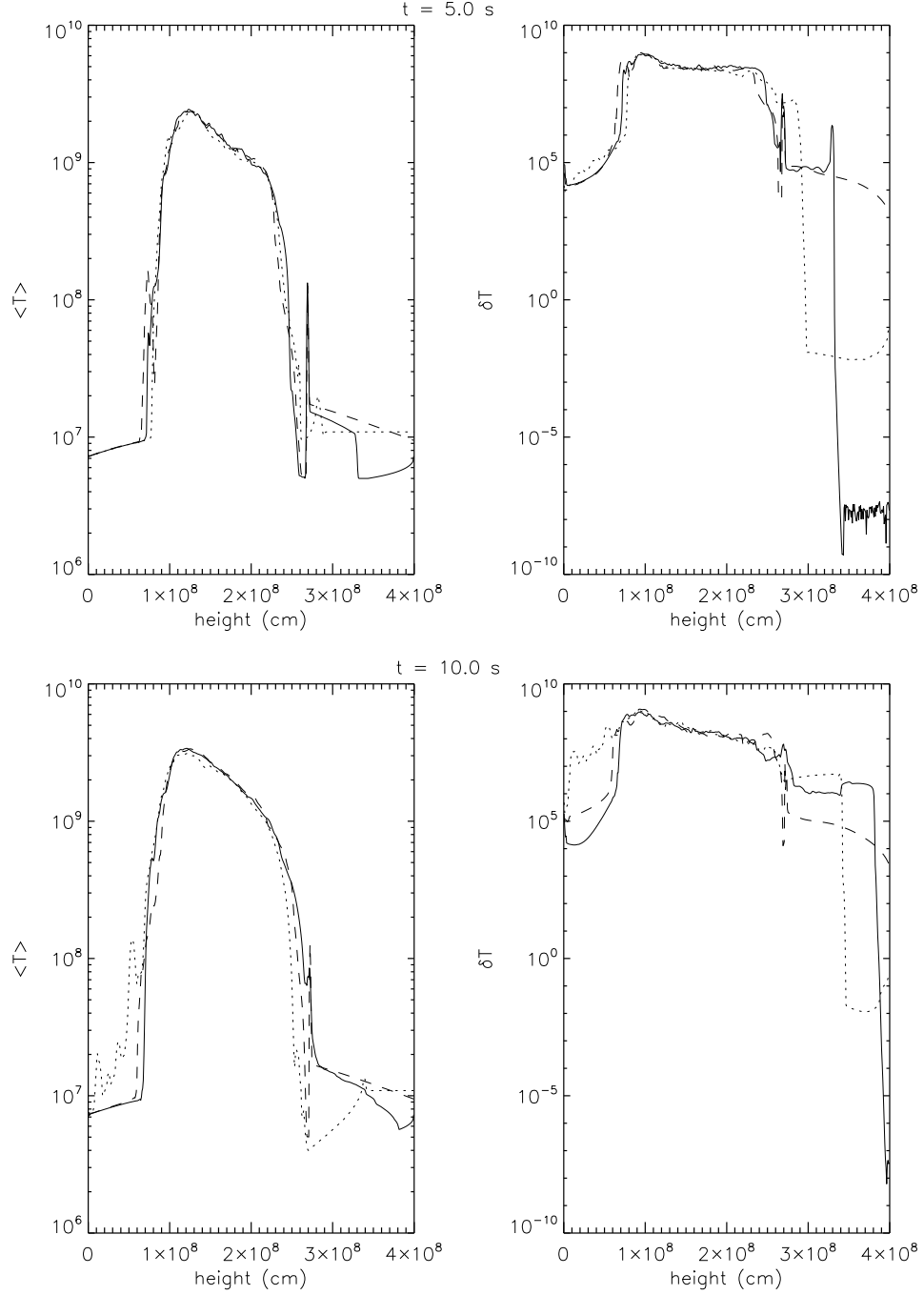


Fig. 5.— Comparison of the average temperature as a function of height, $\langle T \rangle$ and the deviation of temperature from the average, δT , for the compressible (solid), compressible with sponge (dashed) and low Mach with sponge (dotted) calculations. Our region of interest is $10^8 \text{ cm} \leq r \leq 2.2 \times 10^8 \text{ cm}$.

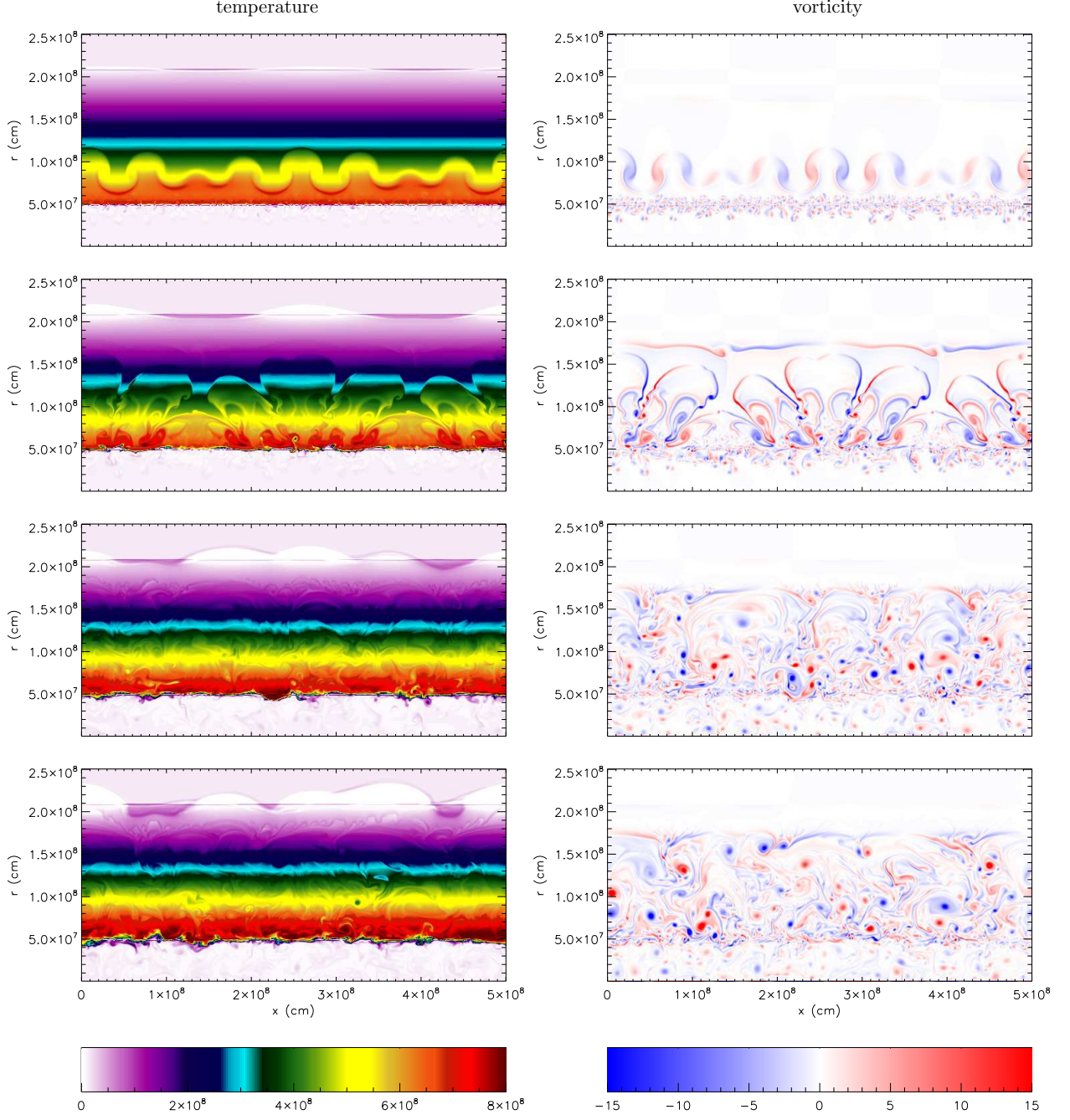


Fig. 6.— Temperature and vorticity evolution for the low heating rate, longtime evolution calculation, shown (from top to bottom) at 15, 20, 40, and 60 s.

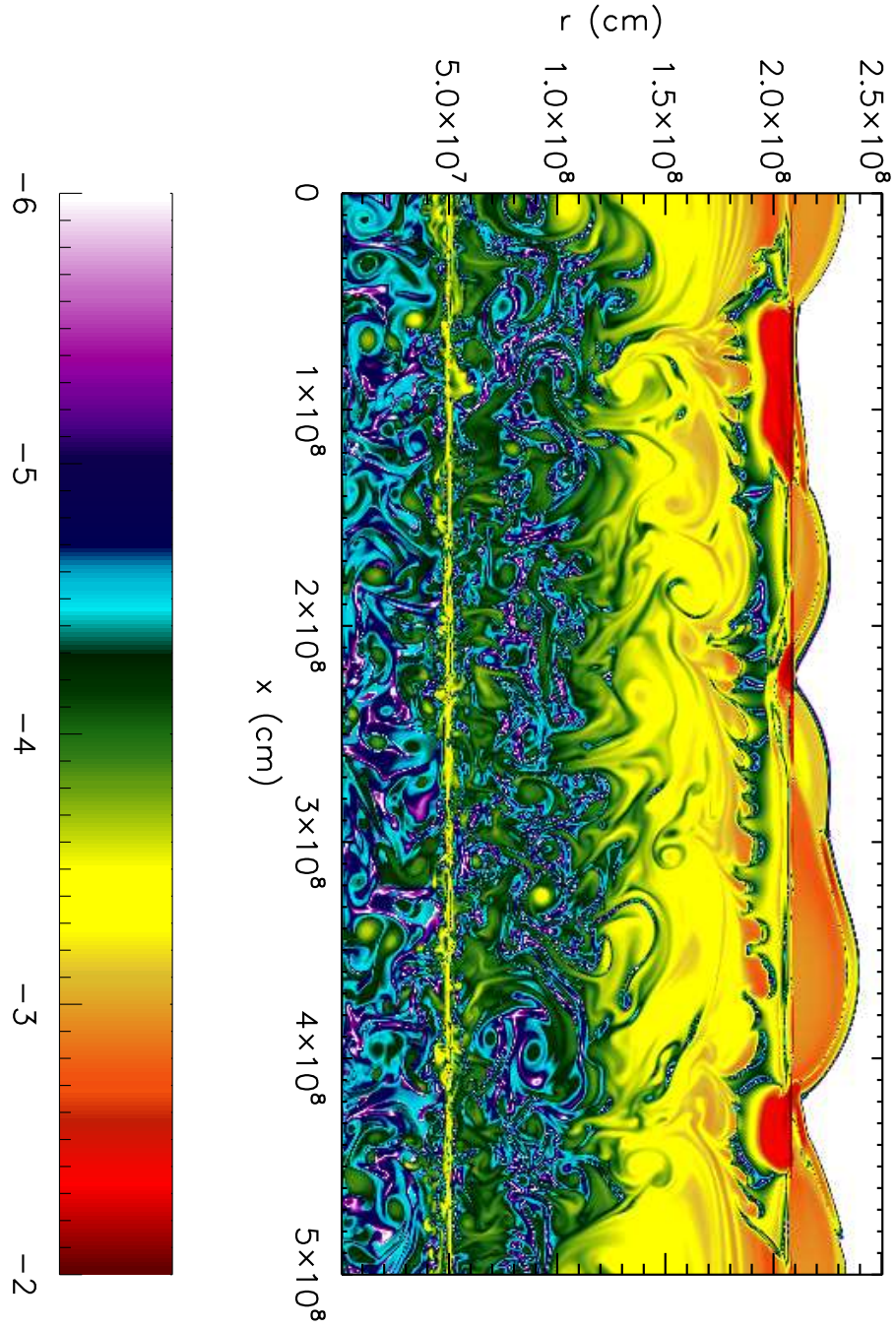


Fig. 7.— Plot of $\log[|(\delta p)_{\text{drift}}|/p_0]$ at $t = 60$ s.

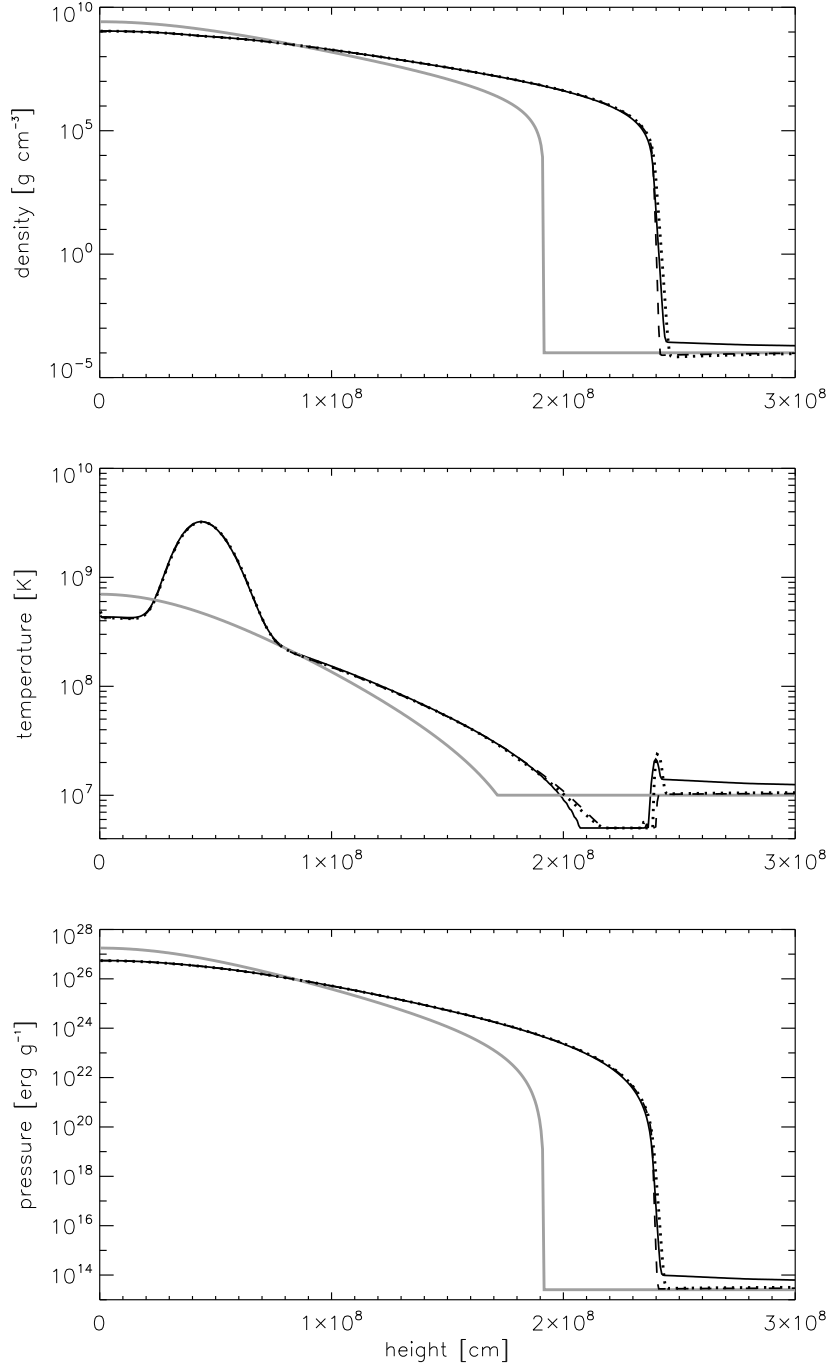


Fig. 8.— Hydrostatic adjustment of a spherically symmetric white dwarf with self-gravity. The gray line represents the initial model; all other lines are after 10 s of heating. The solid black line is the fully compressible solution, the dotted line is the low Mach number solution with a CFL number of 0.5, and the dashed line is the low Mach number solution with a CFL number of 0.1. All simulations used 768 equally spaced zones. We see excellent agreement between the compressible and low Mach number models. The only differences appear at the top of the atmosphere, where the outer boundary condition can influence the results.